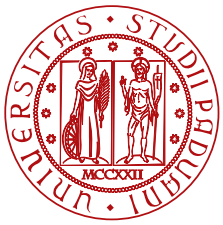

UNIVERSITÀ DEGLI STUDI DI PADOVA

DIPARTIMENTO DI INGEGNERIA DELL'INFORMAZIONE


DIPARTIMENTO DI INGEGNERIA DELL'INFORMAZIONE

CORSO DI LAUREA IN INGEGNERIA DELL'AUTOMAZIONE


# Zero-speed rotor position reconstruction techniques analysis for hybrid excitation PM motors


**Relatore**
Prof. Bianchi Nicola

**Laureando**
Dalla Zuanna Edoardo

**Correlatore**
Carlet Gherardo Paolo



ANNO ACCADEMICO 2023-2024

Data di laurea 16/04/2024

**Sommario**

In condizioni di funzionamento a bassa velocità, le tecniche di stima sensorless offrono un'ottima alternativa ai metodi convenzionali sensored. Questa tesi presenta un'analisi comparativa focalizzata sulla valutazione dell'efficacia dei metodi di stima a bassa velocità basati sull'analisi di corrente di rotore e di statore per la stima della velocità e della posizione del motore nel contesto dei motori a Magneti Permanenti ad Eccitazione Ibrida (HEPM). Le basi teoriche di queste due tecniche di stima sensorless sono trattate nel dettaglio, enfatizzandone il funzionamento per questo particolare tipo di motori. Con lo scopo di validare queste teorie, una serie di simulazioni sul modello matematico del motore sono state effettuati. Ogni tecnica di stima viene valutata per precisione, robustezza e accuratezza. Inoltre in questo lavoro è stata analizzata l'integrazione con gli algoritmi di controllo e l'adattamento alle caratteristiche dei motori HEPM. I risultati della tesi forniscono un contributo sostanziale alla nostra comprensione delle tecnologie sensorless nel campo dei motori ad eccitazione ibrida, e offrono ad ingegneri e ricercatori una strada per il miglioramento degli azionamenti elettrici. In conclusione, questa tesi offre un'analisi completa delle tecniche di stima sensorless basate sull'iniezione in rotore e statore specificamente progettate per il funzionamento a bassa velocità nei motori a Magneti Permanenti ad Eccitazione Ibrida.

**Abstract**

In low-speed operating scenarios, sensorless estimation techniques offer a feasible alternative to the drawbacks of conventional sensor-based methods. This thesis provides a comparative analysis focused on evaluating the effectiveness of rotor-based and stator-based low-speed sensorless estimate methods for the motor speed and position estimation task in the context of Hybrid Excitation Permanent Magnet (HEPM) motors. The theoretical basis of these two sensorless estimation techniques is covered in detail, focusing on how they are related to HEPM motors. A wide range of simulations and experiments are used to evaluate the performance of the approaches presented. Each estimating technique is evaluated for precision, robustness, and accuracy. Moreover, integration with control algorithms and adaptation to the special features of HEPM motors are examined. The results provide a substantial contribution to our understanding of sensorless technologies in the specialized field of hybrid excitation motors, and they offer engineers and researchers critical direction for improving electric drives. In conclusion, this thesis offers a comprehensive analysis of rotor and stator-based sensorless estimation techniques specifically tailored for low-speed operation in Hybrid Excitation Permanent Magnet motors.

# Contents

**List of Figures** **xi**

**List of Tables** **xiii**

**List of Acronyms** **xv**

**1 Introduction** **1**

**2 Background** **3**
2.1 HEPM motor linearized model . . . . . 3
2.2 Low-speed sensorless estimation . . . . . 5

**3 State-Of-The-Art** **7**
3.1 Stator voltage injection method . . . . . 7
3.2 Park transform reference frame estimation . . . . . 8
3.3 Estimator structure and PI controller design . . . . . 12

**4 Rotor Injection Position Reconstruction** **17**
4.1 High-frequency voltage injection propagation . . . . . 17
4.2 Park transform reference frame estimation . . . . . 18
4.3 PI controller design . . . . . 20

**5 Numerical Validations** **21**
5.1 Simulation setup . . . . . 21
5.2 Stator injection method . . . . . 23
5.2.1 Observer design validation . . . . . 23
5.2.2 Zero-speed and low-speed rotor position reconstruction . 27
5.2.3 Magnetic saturation considered . . . . . 29
5.3 Rotor injection method . . . . . 31

5.3.1 Observer design validation . . . . . 31
5.3.2 Zero-speed and low-speed rotor position reconstruction . 35
5.3.3 Magnetic saturation considered . . . . . 37

**6 Estimated Speed Feedback Control Design** **39**
6.1 Measure filter derivation . . . . . 39
6.2 Control scheme analysis and PID design . . . . . 41

**7 Method Comparison** **45**

**8 Preliminary Experimental Validation** **51**
8.1 Experimental setup . . . . . 51
8.2 Experimental results . . . . . 52

**9 Conclusions** **59**

**10 Appendix** **61**
10.1 Differential inductance matrix inversion . . . . . 61
10.2 Matlab code for current derivation . . . . . 62

# List of Figures


2.1 Block diagram of the HEPM motor model . . . . . 5

3.1 Relation between the true d-q axis and the estimated one . . . . . 9
3.2 Block diagram of the proposed sensor-less position estimator . . . 13
3.3 Comprehensive transfer function scheme used for controller design 14
3.4 Controlled and uncontrolled open-loop observer transfer functions 15

5.1 Motor simulation model setup . . . . . 22
5.2 Injected voltage waveform for sensorless estimation procedure . . 24
5.3 Injected currents behaviors for the stator injection estimation method with theoretical boundaries computed in (5.3) for $\Delta\Theta_m^e = \frac{\pi}{8}$ rad . . . . . 24
5.4 Injected currents behaviors for the stator injection estimation method with theoretical boundaries computed in (5.3) for $\Delta\Theta_m^e = \frac{\pi}{4}$ rad . . . . . 25
5.5 Comparison between the simulated $\hat{I}_q^{hf}(s)$ and the simplified transfer function $G_\theta(s)$ for the stator injection method . . . . . 26
5.6 Error introduced by the simplification in the controller design for the stator injection method . . . . . 26
5.7 Fourier transform of the demodulated q-axis high-frequency error component for the stator injection method . . . . . 27
5.8 Zero-speed rotor position estimation starting from the rotor position $\theta_m^e = \frac{\pi}{4}$ for the stator injection method . . . . . 28
5.9 Zero-speed rotor speed estimation starting from the rotor position $\theta_m^e = \frac{\pi}{4}$ rads for the stator injection method . . . . . 28
5.10 Stator injection low-speed rotor position estimation . . . . . 29
5.11 Stator injection low-speed rotor speed estimation . . . . . 29

5.12 Estimated rotor position from the stator injection-based observer in comparison with the measured rotor position . . . . . 30
5.13 Predicted rotor position reconstruction error in comparison with actual estimation error coming from the stator injection-based observer . . . . . 31
5.14 Excitation winding injected voltage and induced voltage in the d-axis . . . . . 32
5.15 Detail of the voltage in the d-axis induced by the injected voltage 32
5.16 Injected currents behaviors with theoretical boundaries for rotor injection method . . . . . 33
5.17 Comparison between the seimulatad $\hat{I}_q^{hf}(s)$ and the simplified transfer function $G_\theta(s)$ for the rotor injection method . . . . . 34
5.18 Error introduced by the simplification in the controller design for the rotor injection method . . . . . 34
5.19 Fourier transform of the demodulated q-axis high-frequency error component for the rotor injection method . . . . . 35
5.20 Zero-speed rotor position estimation starting from the rotor position $\theta_m^e = \frac{\pi}{4}$ for the rotor injection method . . . . . 35
5.21 Zero-speed rotor speed estimation starting from the rotor position $\theta_m^e = \frac{\pi}{4}$ for the rotor injection method . . . . . 36
5.22 Rotor injection observer low-speed rotor position estimation . . . 36
5.23 Rotor injection observer low-speed rotor speed estimation . . . . 37
5.24 Estimated rotor position from the rotor injection-based observer in comparison with the measured rotor position . . . . . 38
5.25 Predicted rotor position reconstruction error in comparison with actual estimation error coming from the rotor injection-based observer . . . . . 38

6.1 Block diagram of the measure-to-estimated position transfer function . . . . . 40
6.2 Speed feedback control scheme using the estimated speed as the control measure . . . . . 41
6.3 Speed feedback equivalent block scheme . . . . . 42

7.1 Confrontation between the methods measured position reconstruction error and the estimated error coming from the error prediction equations (5.4) and (5.7) . . . . . 45

7.2 Measured speed step response with estimated speed and position feedback controller . . . . . 46
7.3 Measured versus observed electro-mechanical position after error compensation . . . . . 47
7.4 True (dashed) versus estimated position with $\Theta_m^e = 2.09$ rad with the estimation error for stator injection method . . . . . 47
7.5 Measured (dashed) versus estimated position for zero-speed stator injection estimation method with an initial position in proximity of $\theta_{me} = \pi$ . . . . . 48
7.6 Measured (dashed) versus estimated speed for zero-speed stator injection estimation method with an initial position in proximity of $\theta_{me} = \pi$ . . . . . 48
7.7 Measured (dashed) versus estimated position for zero-speed rotor injection estimation method with an initial position in proximity of $\theta_{me} = \pi$ . . . . . 49
7.8 Measured (dashed) versus estimated speed for zero-speed rotor injection estimation method with an initial position in proximity of $\theta_{me} = \pi$ . . . . . 49

8.1 Experimental setup . . . . . 52
8.2 Current propagated inside the experimental setup due to the stator voltage injection . . . . . 53
8.3 Current propagated inside the experimental setup due to the stator voltage injection . . . . . 53
8.4 Measured position compared to the estimated position coming from the stator injection observer while the HEPM motor is driven by the load motor . . . . . 54
8.5 Measured position compared to the estimated position coming from the rotor injection observer while the HEPM motor is driven by the load motor . . . . . 54
8.6 Measured speed compared to the estimated speed coming from the stator injection observer while the HEPM motor is driven by the load motor . . . . . 55
8.7 Measured speed compared to the estimated speed coming from the rotor injection observer while the HEPM motor is driven by the load motor . . . . . 55

8.8 Experimental confrontation between the actual position reconstruction error and the predicted one from equations (5.4) and (5.7) . . . . . 56
8.9 Experimental confrontation between the measured position and the stator injection reconstruction when the observed state is used as feedback for the speed control . . . . . 57
8.10 Experimental confrontation between the measured position error and the error coming from the stator injection method prediction formula when the observed state is used as feedback for the speed control . . . . . 57

# List of Tables

5.1 Proportional, integrative, and derivative control action given a control input $\epsilon(t)$ . . . . . 23

# List of Acronyms

**ODE** Ordinary Differential Equation

**LTI** Linear Time Invariant

**HEPM** Hybrid Excitation Permanent Magnet

**IPM** Internal Permanent Magnet

**LPF** Low Pass Filter

**HPF** High Pass Filter

**MTPA** Maximum Torque Per Ampere

**PID** Proportional Integrative Derivative

# 1

# Introduction

Permanent magnet motor development dates back to the early 19th century. However, high-performance applications had to wait for significant advances in materials and technology which did not come until the middle of the 20th century. Creating magnetic fields using permanent magnets rather than conventional electromagnets was the key idea behind developing machines that could achieve high mechanical performances. Early applications of permanent magnet motors were limited due to the available materials, such as alnico and ferrite magnets [1]. Permanent magnet motors didn't show their true potential until the discovery and commercialization of rare earth magnets, such as neodymium-iron-boron (NdFeB) [2] and samarium cobalt (SmCo) [3]. Permanent magnet motors are among the technologies responsible for the evolution of many industrial applications, especially the automotive sector and industrial automation. The main uses for these motors are electric and hybrid car propulsion, providing unmatched energy efficiency and power density. Moreover, permanent magnet motors granted more precise and effective motion control systems, increasing manufacturing process efficiency and precision, causing a paradigm shift in the whole industrial landscape. This technology is concurrently adopted by high-performance industries including aerospace and robotics thanks to their small size, superior controllability, and better torque-to-inertia ratio [4] [5]. Permanent magnet motors set the stage for the development of electric motor technology that hybrid excitation motors represent. Hybrid excitation motors combine the advantages of permanent magnets and electromagnets to provide increased flexibility and controllability. This combination enhances the dynamic control

properties and field weakening with permanent magnets to deliver better power density and control efficiency [6][7][8]. This research presents a sensorless position estimation technique for hybrid excitation permanent magnet (HEPM) motors. Without adopting sensors, the method estimates the position of the rotor using a combination of model-based and signal-processing techniques. This work emphasizes a solution for the low-speed position reconstruction problem. The suggested approach relies on injecting a high-frequency sinusoidal voltage into the rotor winding to measure the currents induced in the motor stator. These currents are used to determine the position and speed of the rotor. This work consists of a comparison between the rotor voltage injection and the stator voltage injection technique. While the latter method is widely used in conventional anisotropic machines and presented in [9] and [10], the former, since is applicable only for HEPM motor, presents a possible improvement to the observer performances. The work also includes the validation procedure analyzing the outcome of the simulations performed on the motor models, and the actual behavior on the physical machine, showing the results of the comparison between the two strategies.

# 2

# Background

This chapter exploits the knowledge needed to understand the mathematics reported in this thesis. A complete understanding of this chapter is mandatory during the comparison between the two sensorless estimation techniques applicable to the Hybrid Excitation Permanent Magnet (HEMP) Motor.

## 2.1 HEPM motor linearized model

This section presents a brief recap of the theoretical background reported in [11]. Adopting the Park transform it is possible to rewrite the three-phase alternate voltages applied to the motor stator, $i_a$, $i_b$ and $i_c$ into the d-q reference frame. This new reference frame is used for the motor control and the voltage-current equations. Omitting the effect of spatial-flux linkage harmonics and temperature, in (2.1) is exploited the voltage to current ODE.

$$\begin{cases} \dfrac{\mathrm{d}\lambda_d\left(i_{dqe}(t)\right)}{\mathrm{d}t} = u_d(t) - R_s i_d(t) - \omega_m^e(t)\lambda_q\left(i_{dqe}(t)\right) \\ \dfrac{\mathrm{d}\lambda_q\left(i_{dqe}(t)\right)}{\mathrm{d}t} = u_q(t) - R_s i_q(t) + \omega_m^e(t)\lambda_d\left(i_{dqe}(t)\right) \\ \dfrac{\mathrm{d}\lambda_e\left(i_{dqe}(t)\right)}{\mathrm{d}t} = u_e(t) - R_e i_e(t) \end{cases} \tag{2.1}$$

With $u_d$, $u_q$ and $i_d$, $i_q$ being the d-q stator voltage and current components expressed after the Park transform. Moreover, the $u_e$, $i_e$ are the excitation coil voltage and current. As a convention, we describe the vectorial form for the current as $i_{dqe}(t) = [i_d(t) \quad i_q(t) \quad i_e(t)]^T$. The rotor flux linkage $\lambda_d\left(i_{dqe}(t)\right)$, $\lambda_q\left(i_{dqe}(t)\right)$ and $\lambda_e\left(i_{dqe}(t)\right)$ depends on the motor operation point. Rewriting (2.1) in compact matrix form, (2.2) is derived.

$$\frac{\mathrm{d}\lambda_{dqe}\left(i_{dqe}(t)\right)}{\mathrm{d}t} = \frac{\mathrm{d}}{\mathrm{d}t}\begin{bmatrix}\lambda_d\left(i_{dqe}(t)\right)\\ \lambda_q\left(i_{dqe}(t)\right)\\ \lambda_e\left(i_{dqe}(t)\right)\end{bmatrix} = \begin{bmatrix}u_d(t)\\ u_q(t)\\ u_e(t)\end{bmatrix} - R\begin{bmatrix}i_d(t)\\ i_q(t)\\ i_e(t)\end{bmatrix} - \omega_m^e J\begin{bmatrix}\lambda_d(t)\\ \lambda_q(t)\\ \lambda_e(t)\end{bmatrix} \tag{2.2}$$

Matrices used in (2.2) are reported in (2.3).

$$R = \begin{bmatrix}R_s & 0 & 0\\ 0 & R_s & 0\\ 0 & 0 & R_e\end{bmatrix} \qquad J = \begin{bmatrix}0 & 1 & 0\\ -1 & 0 & 0\\ 0 & 0 & 0\end{bmatrix} \tag{2.3}$$

In (2.3) $R_s$ and $R_e$ are respectively the stator resistance and the excitation winding resistance, while $\omega_m^e$ is the mechanical-electrical rotation speed of the magnetic field in the electric machine. The solution to (2.2) is not trivial since the flux linkage vector is on both the terms of the equation. For this reason in order to get a solution for the ODE, an inverse model based on the current description has been used. This current-based model representation is obtained by applying the chain rule to (2.2) and substituting the flux linkage by a function of the motor currents (2.4). This new function $L\left(i_{dqe}(t)\right)$ is exploited in (2.5). Being the current-to-flux linkage characteristics nonlinear, all the matrix components depend on the motor operating conditions.

$$\frac{\mathrm{d}\lambda\left(i_{dqe}(t)\right)}{\mathrm{d}i_{dqe}(t)}\frac{\mathrm{d}i_{dqe}(t)}{\mathrm{d}t} = u_{dqe}(t) - Ri_{dqe}(t) - \omega_m^e J\lambda\left(i_{dqe}(t)\right) \tag{2.4}$$

$$L\left(i_{dqe}(t)\right) = \frac{\mathrm{d}\lambda\left(i_{dqe}(t)\right)}{\mathrm{d}i_{dqe}(t)} = \begin{bmatrix}l_{dd} = \frac{\partial\lambda_d}{\partial i_d} & l_{dq} = \frac{\partial\lambda_d}{\partial i_q} & l_{de} = \frac{\partial\lambda_d}{\partial i_e}\\ l_{qd} = \frac{\partial\lambda_q}{\partial i_d} & l_{qq} = \frac{\partial\lambda_q}{\partial i_q} & l_{qe} = \frac{\partial\lambda_q}{\partial i_e}\\ l_{ed} = \frac{\partial\lambda_e}{\partial i_d} & l_{eq} = \frac{\partial\lambda_e}{\partial i_q} & l_{ee} = \frac{\partial\lambda_e}{\partial i_e}\end{bmatrix} \tag{2.5}$$

Moreover, for the law of energy conservation:

- $l_{dq} = l_{qd}$
- $l_{ed} = \frac{3}{2} l_{de}$
- $l_{eq} = \frac{3}{2} l_{qe}$

This makes the computation for the $L(i_{dqe})$ easier and exploits its reciprocity. Figure 2.1 reports the block scheme of the model described by (2.4) and (2.5).

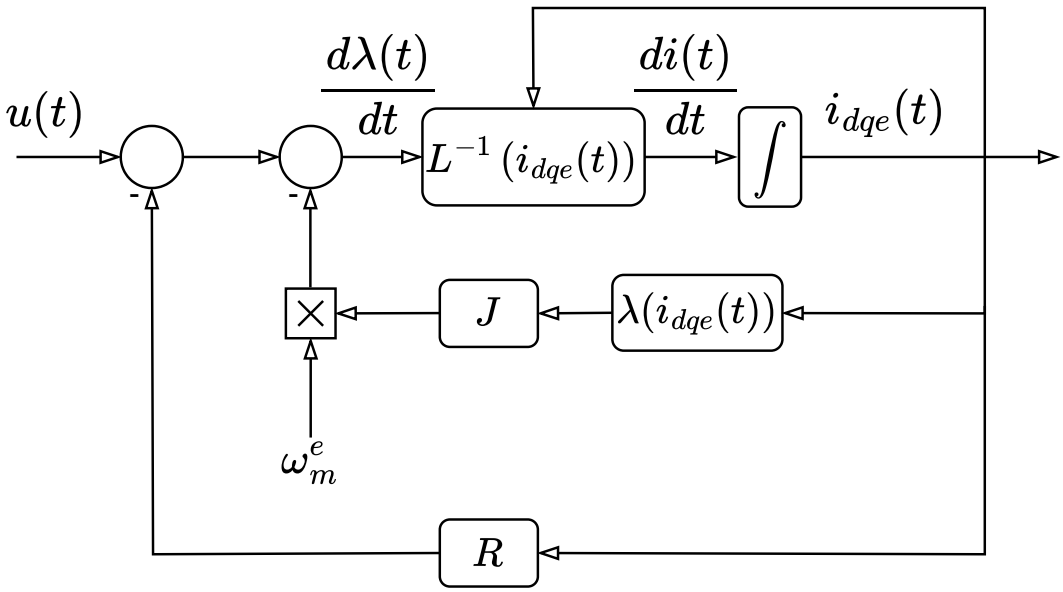


Figure 2.1: Block diagram of the HEPM motor model

## 2.2 Low-speed sensorless estimation

To perform the control action on HEMP motors it is mandatory to know the exact position of the rotor magnet. To precisely calculate the location and speed of the rotor, Sensor-based control techniques rely on data coming from sensors, such as encoders or Hall-effect sensors. With the use of this exact information, controls can be steady and accurate, resulting in superior performance at slow speeds and with changing loads. However, these sensors increase the system's cost and complexity and the dependability of the system may be impacted by their sensitivity to the environment. On the other hand, Sensorless control techniques do not require any physical sensors since they use algorithms to predict the location and speed of the rotor from measurements of back-emf,

voltage, and current. By eliminating sensor-related failure sites, this method decreases hardware complexity and expense while also improving system robustness. However, in low-speed operations scenarios sensorless estimation is feasible only for machines that exploit high anisotropy [12]. In particular, defining the incremental inductances $L_\Sigma(i_d, i_q, i_e)$ and $L_\Delta(i_d, i_q, i_e)$ as in (2.6), in (2.7) is exploited the ration between the major and minor axis of the current response to the high frequency rotating voltage injection. This ratio is also called the saliency ratio.

$$\begin{aligned} L_\Sigma(i_d, i_q, i_e) &= \frac{l_{qq}(i_d, i_q, i_e) + l_{dd}(i_d, i_q, i_e)}{2} \\ L_\Delta(i_d, i_q, i_e) &= \frac{l_{qq}(i_d, i_q, i_e) - l_{dd}(i_d, i_q, i_e)}{2} \end{aligned} \tag{2.6}$$

$$\xi(i_d, i_q, i_e) = \frac{L_\Sigma(i_d, i_q, i_e) + \sqrt{L_\Delta^2(i_d, i_q, i_e) + l_{dq}^2(i_d, i_q, i_e)}}{L_\Sigma(i_d, i_q, i_e) - \sqrt{L_\Delta^2(i_d, i_q, i_e) + l_{dq}^2(i_d, i_q, i_e)}} \tag{2.7}$$

Theoretically, a saliency ratio $\xi > 1$ makes the low-speed sensorless position estimation feasible. For motors meeting this requirement, the sensorless position and speed rotor estimation are performed through the injection of high-frequency voltages in the stator winding. Two main high-frequency injection strategies can be adopted: the rotating signal injection and the pulsating signal injection. The former consists of a superimposition of the fundamental frequency to the stator reference frame [13]. The latter consists of the injection of the high-frequency signal in one of the estimated synchronous reference frame axes (usually the d-axis)[14]. The pulsating signal injection exhibits superior performance, hence it has been considered as a strategy for the stator injection method [15].

# 3

# State-Of-The-Art

The behavior of currents and voltages in the HEMP model are similar to those of the IPM motor as shown in the simplified motor model in (2.1). Hence the analysis made in [9] has been considered as a starting point for the research. Follows the application of the stator high-frequency injection estimation method for HEMP motor position and speed reconstruction.

## 3.1 Stator voltage injection method

The rotor speed and position estimation are derived by analyzing only the current propagated due to the high-frequency injected voltage. Hence all the low-frequency components of the model are filtered by the first operation of the estimator, as described in Sec. 3.2. This means that the flux contribution of the magnets, the resistance voltage drop, and the back-emf contribution are neglected. The state space model resulting is described in equation (3.1), being the simplified version of the model described in equation (2.2). The matrix describing the inductance behavior, reported in (3.2), is obtained thanks to the linearization procedure described in [11].

$$u^{hf}_{d,q,e}(t) = \begin{bmatrix} u^{hf}_{d}(t) \\ u^{hf}_{q}(t) \\ u^{hf}_{e}(t) \end{bmatrix} = \frac{\mathrm{d}}{\mathrm{d}t} \begin{bmatrix} \lambda^{hf}_{d}(t) \\ \lambda^{hf}_{q}(t) \\ \lambda^{hf}_{e}(t) \end{bmatrix} = [l] \cdot \frac{\mathrm{d}}{\mathrm{d}t} \begin{bmatrix} i^{hf}_{d}(t) \\ i^{hf}_{q}(t) \\ i^{hf}_{e}(t) \end{bmatrix} \tag{3.1}$$

$$[l] = \begin{bmatrix} l_{dd} & l_{dq} & l_{ed} \\ l_{dq} & l_{qq} & l_{qe} \\ \frac{3}{2}l_{de} & \frac{3}{2}l_{qe} & l_e \end{bmatrix} \tag{3.2}$$

To perform the high-frequency injection in the stator winding, among all the possible choices, a cosinusoidal function has been chosen:

$$u_d^{hf}(t) = U_{hf} \cdot cos(\omega_{hf} t) \tag{3.3}$$

This approach, which is the standard way to perform low-position reconstruction in anisotropic motors, grants smoother computation by applying the integration step necessary in order to obtain the current equation. On the other hand, this approach is limited in frequency with respect to other injection techniques, like the square pulse injection. However, for this case of study, the injected frequency of the sinusoidal waveform (1kHz) is an order of magnitude lower than the inverter sampling time (10kHz). This makes feasible the usage of the cosinusoidal function for the position reconstruction algorithm.

## 3.2 Park transform reference frame estimation

The true d-q reference frame is not known and needs to be estimated. The key idea is to consider the estimated reference frame shifted from the true one by an error position defined as $\Delta\theta_m^e = \hat{\theta}_m^e - \theta_m^e$, as showed in Figure 3.1. This means that is it possible to consider two reference frames. The true reference frame ($DQE$), which is unknown and needs to be reconstructed, and the estimated reference frame ($D\hat{Q}E$). If the estimated reference frame is anticipating the true d-q frame, the error is positive, meaning that the estimated frame has to be rotated clockwise. Vice versa, if the true d-q frame is anticipating the estimated one, the error is negative, corresponding to a counterclockwise rotation. This means that is it possible to switch between the two reference frames thanks to the rotation matrix $R$ and $\hat{R}$, respectively the estimated-to-true reference frame rotation and vice versa. These matrices are exploited in (3.4). First of all, it is mandatory to consider that the park transform of the injected voltage used in this method is injected in the estimated reference frame. Equation (3.5) describes

the injected high-frequency voltage reference frameshift.

$$R = \begin{bmatrix} cos(\Delta\theta_m^e) & sin(\Delta\theta_m^e) & 0 \\ -sin(\Delta\theta_m^e) & cos(\Delta\theta_m^e) & 0 \\ 0 & 0 & 1 \end{bmatrix} \qquad \hat{R} = \begin{bmatrix} cos(\Delta\theta_m^e) & -sin(\Delta\theta_m^e) & 0 \\ sin(\Delta\theta_m^e) & cos(\Delta\theta_m^e) & 0 \\ 0 & 0 & 1 \end{bmatrix} \tag{3.4}$$

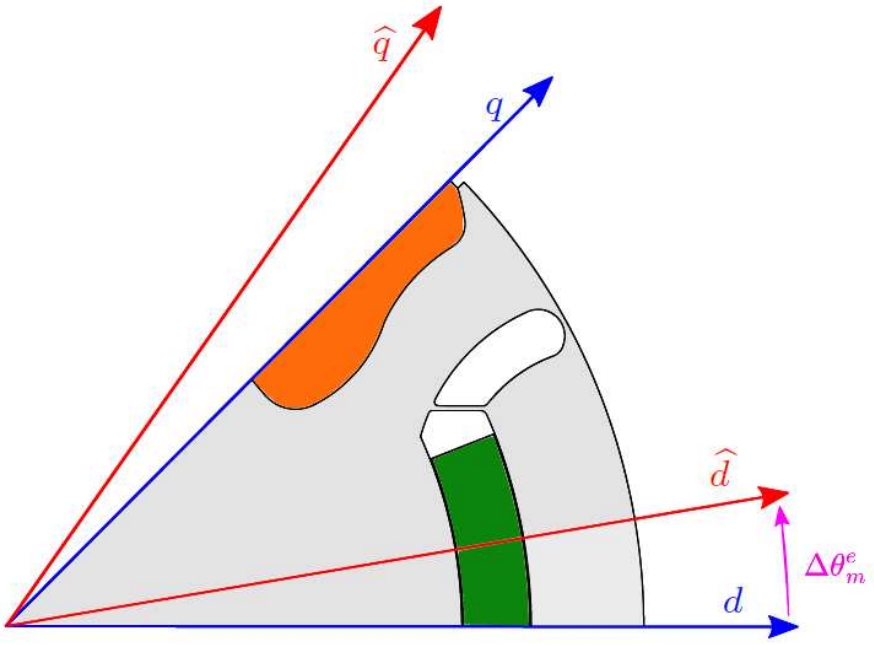


Figure 3.1: Relation between the true d-q axis and the estimated one

$$v_{dqe}^{hf}(t) = R \cdot v_{\hat{dqe}}^{hf}(t) = R \cdot \begin{bmatrix} U_{hf}cos(\omega_{hf}t) \\ 0 \\ 0 \end{bmatrix} = \begin{bmatrix} U_{hf}cos(\Delta_m^e)cos(\omega_{hf}t) \\ -U_{hf}sin(\Delta_m^e)cos(\omega_{hf}t) \\ 0 \end{bmatrix} \tag{3.5}$$

Integrating (3.5) over time, also the rotated flux is derived. This result is exploited in (3.6)

$$\lambda_{dqe}^{hf}(t) = \int u_{dqe}^{hf}(t) \cdot dt = \frac{1}{\omega_{hf}} \begin{bmatrix} U_{hf}cos(\Delta_m^e)sin(\omega_{hf}t) \\ -U_{hf}sin(\Delta_m^e)sin(\omega_{hf}t) \\ 0 \end{bmatrix} \tag{3.6}$$

Combining (3.1) and (3.6) is it possible to extract the behavior of the high-frequency current propagated inside the motor. Moreover, the differential inductances matrix is invertible, as reported in the Appendix. Therefore the

solution for the current exists and it's unique. The current behavior is described in (3.7), with the $\sigma$ term coming from the $[l]$ matrix inversion, also exploited in the appendix.

$$
\begin{aligned}
&i^{hf}_{dqe}(t) = l^{-1} \cdot \lambda^{hf}_{dqe}(t) = \\
&= \frac{1}{l_{qq}\sigma} \begin{bmatrix} 2l_e l_{qq} - 3l_{qe}^2 & 3l_{de}l_{qe} - 2l_{dq}l_e & 2l_{dq}l_{qe} - 2l_{de}l_q \\ 3l_{de}l_{qe} - 2l_{dq}l_e & 2l_{dd}l_e - 3l_{de}^2 & 2l_{de}l_{dq} - 2l_{dd}l_{qe} \\ 3l_{dq}l_{qe} - 3l_{de}l_{qq} & 3l_{de}l_{dq} - 3l_{dd}l_{qe} & 2l_{dd}l_{qq} - 2l_{dq}^2 \end{bmatrix} \cdot \lambda^{hf}_{dqe} = \\
&= \frac{U_{hf} sin(\omega_{hf} t)}{l_{qq}\sigma\omega_{hf}} \begin{bmatrix} cos(\Delta\theta^e_m)(2l_{qq}l_e - 3l_{qe}^2) + sin(\Delta\theta^e_m)(2l_{dq}l_e - 3l_{de}l_{qe}) \\ cos(\Delta\theta^e_m)(3l_{de}l_{qe} - 2l_{dq}l_e) + sin(\Delta\theta^e_m)(3l_{de}^2 - 2l_{dd}l_e) \\ cos(\Delta\theta^e_m)(3l_{dq}l_{qe} - 3l_{de}l_{qq}) + sin(\Delta\theta^e_m)(3l_{dd}l_{qe} - 3l_{de}l_{dq}) \end{bmatrix}
\end{aligned}
\tag{3.7}
$$

However, the Park Transform used to derive the d-q current components described in (3.7) is affected by $\Delta\theta^e_m$, the reconstruction error. Hence the actual estimated high-frequency current is derived by applying the frameshift rotation from the $(DQE)$ to the $(D\hat{Q}E)$ reference frame. This transformationi is introduced in (3.8) multiplying (3.7) by the rotation matrix $\hat{R}$.

$$
i^{hf}_{d\hat{q}e} = \hat{R} \cdot i^{hf}_{dqe}(t) \tag{3.8}
$$

The second component of the estimated current vector (3.8) corresponds to the q-axis current, and has been exploited in (3.9).

$$
i^{hf}_{\hat{q}}(t) = \frac{U_{hf} sin(\omega_{hf} t)}{l_{qq}\sigma\omega_{hf}} \left[\phi(\Delta\theta^e_m) + \mu(\Delta\theta^e_m) + \epsilon(\Delta\theta^e_m)\right] \tag{3.9}
$$

Equation (3.10) reports the components describing the terms of (3.9).

$$
\begin{aligned}
&\phi(\Delta\theta^e_m) = cos^2(\Delta\theta^e_m)(3l_{de}l_{qe} - 2l_{dq}l_{de}) \\
&\mu(\Delta\theta^e_m) = cos(\Delta\theta^e_m) sin(\Delta\theta^e_m)(3l_{de}^2 - 2l_{dd}l_e + 2l_{qq}l_e - 3l_{qe}^2) \\
&\epsilon(\Delta\theta^e_m) = sin^2(\Delta\theta^e_m)(2l_{dq}l_e - 3l_{de}l_{qe})
\end{aligned}
\tag{3.10}
$$

Applying Werner formulas (3.11), equation (3.10) is simplified, obtaining (3.12).

$$\begin{aligned} cos^2(\Delta\theta_m^e) &= \frac{1}{2}(1 + cos(2\Delta\theta_m^e)) \\ sin^2(\Delta\theta_m^e) &= \frac{1}{2}(1 - cos(2\Delta\theta_m^e)) \\ sin(\Delta\theta_m^e)cos(\Delta\theta_m^e) &= \frac{1}{2}sin(2\Delta\theta_m^e) \end{aligned} \tag{3.11}$$

$$i_{\hat{q}}^{hf}(t) = \frac{U_{hf}sin(\omega_{hf}t)}{l_{qq}\sigma\omega_{hf}}\left[\zeta(\Delta\theta_m^e) + \nu(\Delta\theta_m^e)\right] \tag{3.12}$$

Equation (3.13) reports equation (3.12) terms simplified with the Werner formulas.

$$\begin{aligned} \zeta(\Delta\theta_m^e) &= cos(2\Delta\theta_m^e)\left(3l_{de}l_{qe} - 2l_{dq}l_e\right) \\ \nu(\Delta\theta_m^e) &= sin(2\Delta\theta_m^e)\left(\frac{3}{2}\left(l_{de}^2 - l_{qe}^2\right) - l_e\left(l_{dd} - l_{qq}\right)\right) \end{aligned} \tag{3.13}$$

The q-axis component of the estimated high-frequency current is the key behind the sensorless observer because of its relation with the estimation error. On the other hand, as reported in [15], both the cross-coupling differential inductances $l_{qe}$ and $l_{dq}$ have been neglected. Regarding the former, the q-axis is by construction orthogonal to the excitation magnetic field. The cross-coupling differential induction between these two axes is almost zero. For the latter, this assumption holds in motors that show negligible cross saturation. HEPM motors, as shown in [15] suffer from magnetic saturation. However, this assumption simplifies the equation, making the controller design feasible. This hypothesis is going to be relaxed in a later analysis. Under this assumption, the estimated q-axis current is simplified in (3.14) with $\alpha = -3l_{de}^2 + 2l_{dd}l_e$ computed by substituting $l_{dq} = l_{qe} = 0$ in the $\sigma$ term. It is possible to notice that if the estimated d-q axis matches the real ones, $i_{\hat{q}}(t)$ defined as in (3.14) becomes zero. The position observer maps the current error into the position error. For this purpose, taking inspiration from [9], a demodulation procedure based on Werner formulas (3.11) has been performed on the estimated q-axis current, exploited in (3.15). This procedure exploits two components of the q-axis current: one low-frequency component depending only on the reference frame estimation error $\Delta\Theta_m^e$ and a

high-frequency component depending also on the voltage injection frequency.

$$\begin{aligned} i_{\hat{q}}^{hf}(t) &= \frac{U_{hf} sin(\omega_{hf} t)}{l_{qq} \alpha \omega_{hf}} \left[ sin(2\Delta\theta_m^e) \left( \frac{3l_{de}^2}{2} - l_e l_{dd} + l_e l_{qq} \right) \right] \\ &= \cancel{l_{qq}} l_e \left( 1 - \frac{\alpha}{2 l_{qq} l_e} \right) \frac{U_{hf} sin(\omega_{hf} t)}{\cancel{l_{qq}} \alpha \omega_{hf}} sin(2\Delta\theta_m^e) \\ &= \frac{(2 l_{qq} l_e - \alpha) U_{hf} sin(\omega_{hf} t) \cancel{l_e}}{2 \cancel{l_e} l_{qq} \alpha \omega_{hf}} sin(2\Delta\theta_m^e) = \\ &= \frac{(2 l_{qq} l_e - \alpha) U_{hf} sin(\omega_{hf} t)}{2 l_{qq} \alpha \omega_{hf}} sin(2\Delta\theta_m^e) \end{aligned} \tag{3.14}$$

Applying a low pass filter with a cut-off frequency near the injection frequency to the demodulated estimated q-axis current, the dependency from $\omega_{hf}$ in (3.15) is eliminated.

$$\begin{aligned} i_{\hat{q}}^{hf}(t) sin(\omega_{hf} t) &= \frac{\left(2 l_{qq} l_e - \alpha\right) U_{hf} sin^2(\omega_{hf} t)}{2 l_{qq} \alpha \omega_{hf}} sin(2\Delta\theta_m^e) \\ &= \frac{\left(l_{qq} l_e - \alpha\right) U_{hf}}{4 l_{qq} \alpha \omega_{hf}} \left[ sin(2\Delta\theta_m^e) - sin(2\Delta\theta_m^e) cos(2\omega_{hf} t) \right] \end{aligned} \tag{3.15}$$

Moreover (3.15) is linearizable around the working point $\Delta\theta_m^e = 0$ getting (3.16).

$$\hat{i}_{\hat{q},demod}^{hf} = \frac{\left(2 l_{qq} l_e - \alpha\right) U_{hf}}{4 l_{qq} \alpha \omega_{hf}} sin(2\Delta\theta_m^e)\Big|_{\Delta\theta_m^e = 0} \approx \frac{\left(2 l_{qq} l_e - \alpha\right) U_{hf}}{2 l_{qq} \alpha \omega_{hf}} \Delta\theta_m^e \tag{3.16}$$

## 3.3 Estimator structure and PI controller design

In (3.16) the correlation between the q-axis demodulated current and the estimated d-q reference frame orientation error is exploited. Hence controlling this quantity to zero grants the correct estimation of the d-q reference frame. The rotor position estimator is exploited in the scheme shown in Figure 3.2. Measuring the $\alpha - \beta$ currents, the estimated d-q axis is computed by performing the Park transform with the estimated rotor position $\hat{\theta}_m^e$ coming from the observer. Taking the estimated q-axis current $\hat{i}_q$, the position reconstruction error $\Delta\theta_m^e$ is computed thanks to 3 operations:

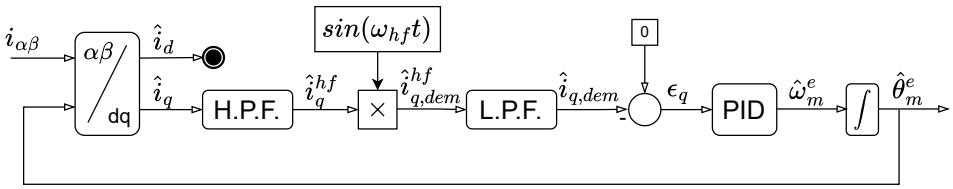


Figure 3.2: Block diagram of the proposed sensor-less position estimator

- High pass filtering, removing the motor control current contribution, obtaining $\hat{i}_q^{hf}(t)$;
- Demodulation using the $sin(\omega_{hf}t)$ function;
- Low pass filtering, removing the high-frequency term introduced by the demodulation;

The signal coming from the procedure above is proportional to the d-q reference frame estimation error, as shown in (3.15). This measure is now compared to the desired value 0, giving the error $\epsilon_q$. This error is used to generate the estimated speed $\hat{\omega}_{me}$ by a proportional integrative action (PI controller). Then the estimated speed is integrated resulting in the estimated position $\hat{\theta_m^e}$. Hence this position is used as feedback for the Park transform. The transfer function describing the relation between the high-frequency estimated q-axis current and the reconstruction error $\Delta\theta_m^e$ has been obtained and shown in (3.17). The mathematical result is proved in [9]. This transfer function is composed of a series of LTI systems: The LPF transfer function in (3.18), the HPF transfer function in (3.19), and eventually the transfer function reporting the demodulation effect by the perspective of the HPF transfer function in (3.20). In these equations $\tau_{lpf}$ and $\tau_{hpf}$ are respectively the low pass filter and high pass filter time constants, while $\omega_{lpf}$ and $\omega_{hpf}$ are the filters cut-off frequencies, expressed in rad/s.

$$G_{\hat{\omega}}(s) = \frac{I_q^{hf}(s)}{\Delta\Theta_m^e(s)} = \frac{\left(2l_{qq}l_e - \alpha\right)U_{hf}}{2l_{qq}\alpha\omega_{hf}} \cdot H_{LPF}(s) \cdot H_{HPF}^{\Sigma}(s) \tag{3.17}$$

$$H_{LPF}(s) = \frac{1}{1+\tau_{lpf}s} \tag{3.18}$$

$$H_{HPF}(s) = \frac{\tau_{hpf}s}{1+\tau_{hpf}s} \tag{3.19}$$

$$H_{HPF}^{\Sigma}(s) = \frac{H_{HPF}(s+j\omega_{hpf}) + H_{HPF}(s-j\omega_{hpf})}{2} \tag{3.20}$$

In Figure 3.3 is shown the block scheme describing the simplified behavior of the estimator. The comprehensive open-loop transfer function is exploited in (3.21).

$$G_{\hat{\theta}}(s) = \frac{G_{\hat{\omega}}(s)}{s} = \frac{\left(2l_{qq}l_e - \alpha\right) U_{hf}}{2l_{qq}\alpha\omega_{hf}s} \cdot H_{LPF}(s) \cdot H^{\Sigma}_{HPF}(s) \tag{3.21}$$

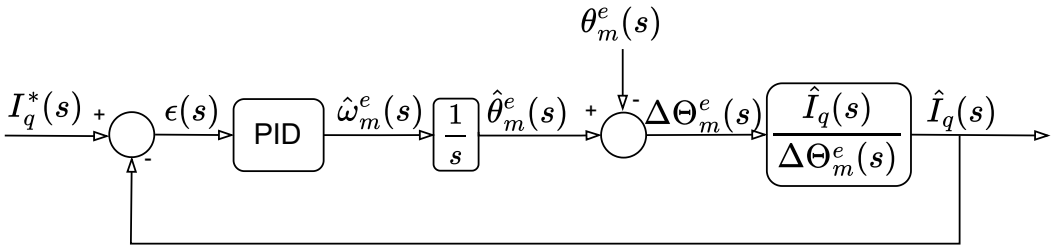


Figure 3.3: Comprehensive transfer function scheme used for controller design

The first step to have an easier design with the bode method is to normalize the gain in (3.17). The compensation gain is exploited in (3.22).

$$K_R = \frac{2l_{qq}\alpha\omega_{hf}}{(2l_{qq}le - \alpha)U_{hf}} \tag{3.22}$$

In Figure 3.3 the true position $\theta^e_m$ is acting like an actuation disturbance. Thanks to the internal model principle, the feedback control action is capable of disturbance rejection if the dynamics of that particular disturbance are present inside the open loop comprehensive transfer function. In steady-state conditions, the true position has a ramp-like behavior, which has dynamics described by a double pole in zero [9]. Hence, since inside the transfer function in (3.21) is already present one pole in zero, the regulator must contain a pole in zero to compensate for the unknown true position action disturbing the control task. For this purpose, a PI controller has been considered. The frequency domain requirements for the controlled systems are:

- Cut-off frequency $\omega_{gc} = 40\pi\ rad/s$, corresponding to a f = 20 Hz control band with;
- Phase margin $\phi = 60°$;

This corresponds to a design rise time of 17.5ms for the feed-back controlled system. The controller synthesis has been performed thanks to the open-loop

Bode method. Figure 3.4 shows both the controlled and uncontrolled open-loop observer transfer functions.

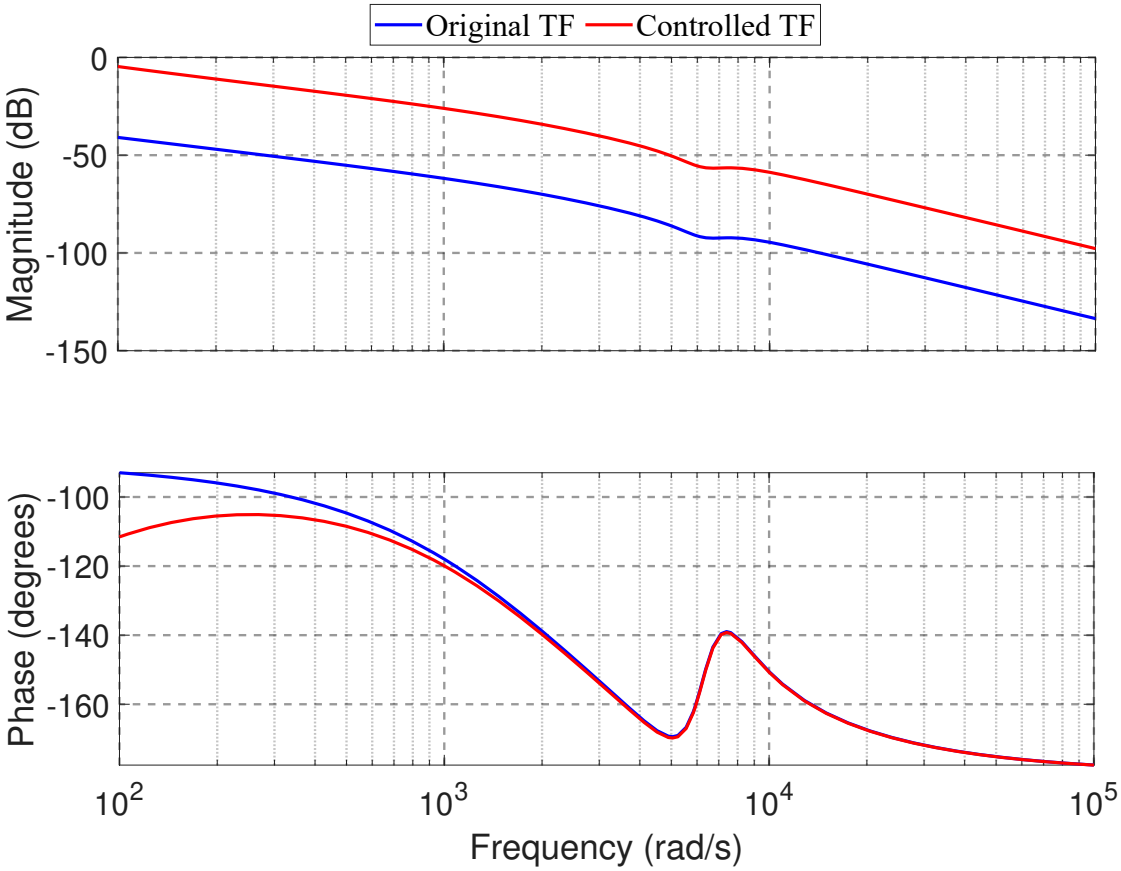


Figure 3.4: Controlled and uncontrolled open-loop observer transfer functions

# 4

# Rotor Injection Position Reconstruction

## 4.1 High-frequency voltage injection propagation

Thanks to the construction proprieties exploited in Sec. 2.1, a different approach for the speed and position observer than the stator high-frequency voltage injection is proposed. In this section is explained the mathematical behavior that makes feasible the position and speed reconstruction method based on pulsating rotor high-frequency voltage injection. The injected voltage waveform and the mathematical model for the motor remain the same. However voltage dynamics equation has to be rewritten considering that the waveform is now injected in the rotor winding, leading to equation (4.1).

$$\frac{\mathrm{d}}{\mathrm{d}t}\begin{bmatrix} i_d^{hf}(t) \\ i_q^{hf}(t) \\ i_e^{hf}(t) \end{bmatrix} = [l]^{-1} \cdot \begin{bmatrix} u_d^{hf}(t) \\ u_q^{hf}(t) \\ u_e^{hf}(t) \end{bmatrix} = [l]^{-1} \cdot \begin{bmatrix} 0 \\ 0 \\ U_{hf} \cdot cos(\omega_{hf} t) \end{bmatrix} \tag{4.1}$$

The Currents propagated in the motor by the high-frequency injected voltage are derived by integrating (4.1) over time. This integration step, similarly as already discussed for the stator injection method in Sec. 3.1, describes the mathematical relationship between the high-frequency voltage injected in the rotor and the currents induced in the stator. This relationship is reported in (4.2), where $\sigma$ is

defined the same as for the stator injection method, exploited in the appendix.

$$\begin{bmatrix} i_d^{hf}(t) \\ i_q^{hf}(t) \\ i_e^{hf}(t) \end{bmatrix} = \int [l]^{-1} \cdot u_{d,q,e}^{hf}(t) \cdot dt = [l]^{-1} \cdot \lambda_{dqe}^{hf}(t) =$$

$$= \frac{1}{l_{qq}\sigma} \begin{bmatrix} 2l_e l_{qq} - 3l_{qe}^2 & 3l_{de}l_{qe} - 2l_{dq}l_e & 2l_{dq}l_{qe} - 2l_{de}l_q \\ 3l_{de}l_{qe} - 2l_{dq}l_e & 2l_{dd}l_e - 3l_{de}^2 & 2l_{de}l_{dq} - 2l_{dd}l_{qe} \\ 3l_{dq}l_{qe} - 3l_{de}l_{qq} & 3l_{de}l_{dq} - 3l_{dd}l_{qe} & 2l_{dd}l_{qq} - 2l_{dq}^2 \end{bmatrix} \cdot \lambda_{dqe}^{hf}(t) = \quad (4.2)$$

$$= \frac{U_{hf} sin(\omega_{hf} t)}{l_{qq}\sigma\omega_{hf}} \cdot \begin{bmatrix} 2l_{dq}l_{qe} - 2l_{de}l_{qq} \\ 2l_{de}l_{dq} - 2l_{dd}l_{qe} \\ 2l_{dd}l_{qq} - 2l_{dq}^2 \end{bmatrix}$$

## 4.2 Park transform reference frame estimation

Equation (4.3) describes the estimated d-q-e currents.

$$\begin{bmatrix} \hat{i}_d^{hf}(t) \\ \hat{i}_q^{hf}(t) \\ \hat{i}_e^{hf}(t) \end{bmatrix} = \hat{R} \cdot \begin{bmatrix} i_d^{hf}(t) \\ i_q^{hf}(t) \\ i_e^{hf}(t) \end{bmatrix} = \hat{R} \cdot \frac{U_{hf} sin(\omega_{hf} t)}{l_{qq}\sigma\omega_{hf}} \cdot \begin{bmatrix} 2l_{dq}l_{qe} - 2l_{de}l_{qq} \\ 2l_{de}l_{dq} - 2l_{dd}l_{qe} \\ 2l_{dd}l_{qq} - 2l_{dq}^2 \end{bmatrix}$$

$$= \begin{bmatrix} cos(\Delta\theta_m^e) & -sin(\Delta\theta_m^e) & 0 \\ sin(\Delta\theta_m^e) & cos(\Delta\theta_m^e) & 0 \\ 0 & 0 & 1 \end{bmatrix} \cdot \frac{U_{hf} sin(\omega_{hf} t)}{l_{qq}\sigma\omega_{hf}} \cdot \begin{bmatrix} 2l_{dq}l_{qe} - 2l_{de}l_{qq} \\ 2l_{de}l_{dq} - 2l_{dd}l_{qe} \\ 2l_{dd}l_{qq} - 2l_{dq}^2 \end{bmatrix} = \quad (4.3)$$

$$= \frac{2U_{hf} sin(\omega_{hf} t)}{l_{qq}\sigma\omega_{hf}} \cdot \begin{bmatrix} cos(\Delta\theta_m^e)(l_{dq}l_{qe} - l_{de}l_{qq}) - sin(\Delta\theta_m^e)(l_{de}l_{dq} - l_{dd}l_{qe}) \\ cos(\Delta\theta_m^e)(l_{de}l_{dq} - l_{dd}l_{qe}) - sin(\Delta\theta_m^e)(l_{de}l_{qq} - l_{dq}l_{qe}) \\ l_{dd}l_{qq} - l_{dq}^2 \end{bmatrix}$$

The first difference between the rotor-based and the stator-based injection observers is that the excitation axis is always aligned with the d-axis for construction. Therefore in the former estimation method, the high-frequency voltage is injected in the real position reference frame. The excitation axis is invari-

ant to the Park transform. However, since the q-axis current used as input for the position estimation is computed by applying the Park transform with the estimated reference frame, the estimation error $\Delta\Theta_m^e$ still affects the current estimation. As already done for the stator injection method, we extract from the estimated currents vector the second component, corresponding to the q-axis current. Also for this estimation method, the cross-coupling inductances $l_{dq}$ and $l_{qe}$ are considered to be zero. This hypothesis is going to be relaxed in later analysis and makes the controller computation simpler. Under this assumption, the high-frequency q-axis current is described by (4.4).

$$\begin{aligned}\hat{i}_q^{hf}(t) &= -\frac{2U_{hf}sin(\omega_{hf}t)l_{de}\cancel{l_{qq}}}{\cancel{l_{qq}}\alpha\omega_{hf}}sin(\Delta\theta_m^e) = \\ &= -\frac{2U_{hf}sin(\omega_{hf}t)l_{de}}{\alpha\omega_{hf}}sin(\Delta\theta_m^e)\end{aligned} \tag{4.4}$$

Moreover, the high-frequency q-axis current is multiplied by $sin(\omega_{hf}t)$ to perform the demodulation [9]. After that, thanks to the Werner formulas described in equation (3.11) the current equation is simplified in (4.5).

$$\begin{aligned}\hat{i}_q^{hf} \cdot sin(\omega_{hf}t) &= -\frac{2U_{hf}l_{de}}{\omega_{hf}\alpha}sin^2(w_{hf}t)sin(\Delta\theta_m^e) \\ &= -\frac{\cancel{2}U_{hf}l_{de}}{\omega_{hf}\alpha}\cdot\frac{1}{\cancel{2}}\left[1-cos(2\omega_{hf}t)\right]sin(\Delta\theta_m^e) \\ &= -\frac{U_{hf}l_{de}}{\omega_{hf}\cdot\alpha}\left[sin(\Delta\theta_m^e)+sin(\Delta\theta_m^e)cos(2\omega_{hf}t)\right]\end{aligned} \tag{4.5}$$

Filtering (4.5) with an LPF it is possible to remove the high-frequency component of the demodulated current. After this operation, only the low-frequency component of the demodulated signal remains. This component as for the stator injection method, is directly correlated with the reference frame estimation error. In (4.6) is performed the linearization step, since the demodulated current is under the linearization condition exploited in Sec.3.2.

$$\hat{i}_{q,demod}^{hf} = -\frac{U_{hf}\cdot l_{de}}{\omega_{hf}\cdot\alpha}\cdot sin(\Delta\theta_m^e)\big|_{\Delta\theta_m^e=0} \approx -\frac{U_{hf}\cdot l_{de}}{\omega_{hf}\cdot\alpha}\cdot\Delta\theta_m^e \tag{4.6}$$

## 4.3 PI CONTROLLER DESIGN

Equation (4.6) describes the relation between the q-axis demodulated current and the estimated d-q reference frame for the rotor injection method. Zeroing this equation the reconstruction error $\Delta\theta_m^e$ becomes zero. The estimator structure described for the stator injection method in Figure 3.2 is the same also for the rotor injection method. The comprehensive transfer function for the rotor injection method has been widely discussed in Sec. 3.3 since the d-q reference frame estimation procedure is the same as for the stator injection estimation method. The control scheme remains the same, as described in Figure 3.3. The transfer function describing the relation between the estimated q-axis current and the reconstruction error $\Delta\theta_m^e$ is reported in (4.7). The filter transfer functions are exploited in (3.18), (3.19) and (3.20). In (4.8) is presented the comprehensive transfer function which presents also the integral action in the position reconstruction procedure.

$$G_{\hat{\omega}}(s) = \frac{I_q^{hf}(s)}{\Delta\Theta_m^e(s)} = -\frac{U_{hf} l_{de}}{\omega_{hf}\alpha} \cdot H_{LPF}(s) \cdot H_{HPF}^{\Sigma}(s) \tag{4.7}$$

$$G_{\hat{\theta}}(s) = \frac{G_{\hat{\omega}}(s)}{s} = \frac{I_q^{hf}(s)}{s\Delta\Theta_m^e(s)} = -\frac{U_{hf} l_{de}}{s\omega_{hf}\alpha} \cdot H_{LPF}(s) \cdot H_{HPF}^{\Sigma}(s) \tag{4.8}$$

Regarding the observer regulator, the control architecture remains the same since once the gain in (4.8) is compensated both the estimation methods present the same transfer function and block scheme characteristics. The compensation gain is reported in (4.9). This normalization allows the use of the same PI design as in Sec.3.3. The bode diagram of the controlled transfer function remains the same as the rotor injection method, shown in Figure 3.4.

$$K_R = -\frac{\omega_{hf} \cdot \alpha}{U_{hf} l_{de}} \tag{4.9}$$

# 5 Numerical Validations

## 5.1 Simulation setup

The simulation model used for all the numerical validations has been created using the theoretical knowledge provided in [6] and [7]. Strategy for motor control is exploited in [16]. This strategy is also applicable to the excitation controller $PI_e$. In (5.1) is reported the PI design for the desired current bandwidth $B_w^e = 100Hz$, with $L_e$ and $R_e$ respectively the excitation circuit inductance and resistance.

$$\begin{cases} K_p^e = 2\pi \cdot B_w^e \cdot L_e \\ \\ K_i^e = 2\pi \cdot B_w^e \cdot R_e \end{cases} \tag{5.1}$$

Figure 5.1 reports the Simulink block scheme used for the simulation. The model used for representing the motor behavior is the Current-Based Description Model (C.B.D.), described in Sec. IIIB of [11]. This model allows a very flexible simulation setup since the whole motor behavior is encoded in the values of the [l] matrix. With this model, it is possible to switch on and off the magnetic saturation effect and see the correlation between the measured high-frequency currents and the rotor position-speed observer behavior. Observer simulink realization follows exactly the scheme described in Figure 3.2.

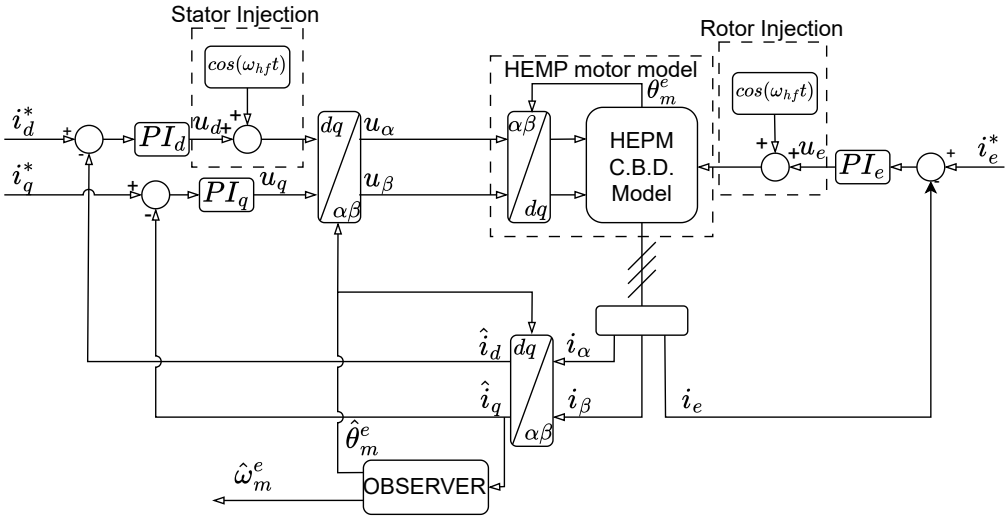


Figure 5.1: Motor simulation model setup

To get the most accurate reconstruction for the experimental setup, the system has been discretized. All the filter transfer functions have been converted from continuous-time design to discrete-time design by the use of the bilinear transformation (Tustin method). This method remaps the continuous-time s-plane described by the $s$ variable to the discrete-time complex z-plane, described by the $z$ variable. This transformation is performed by substituting the s variable with the expression reported in (5.2), where $T_s$ is the system sampling time. In the HEPM motor experimental setup, the inverter presents a sampling frequency of 20KHz, meaning that $T_s = 50\mu s$.

$$s = \frac{2}{T_s} \cdot \frac{1 - z^{-1}}{1 + z^{-1}} \tag{5.2}$$

Regarding the PID controller discretization, table 5.1 presents the mathematical meaning of the proportional and integral control action given the control error $\epsilon(t)$ and its discrete-time representation $\epsilon(k \cdot T_s)$. In this table, $K_p$, $K_i$, and $K_d$ respectively the proportional, integral, and derivative gains coming from the continuous time PI design. Therefore the PID controller discretization has been achieved by the multiplication of the integral gain $Ki$ for the system sampling time. Regarding the derivative gain, it has to be divided by the sample time while the proportional gain $K_p$ remains the same.

| Control Action | Continous Time | Discrete Time |
|---|---|---|
| Proportional | $K_p \cdot \epsilon(t)$ | $K_p \epsilon(k \cdot T_s)$ |
| Integrative | $K_i \cdot \int_0^t \epsilon(\tau)\, d\tau$ | $K_i \sum_{j=0}^{k} [\epsilon(j \cdot T_s) \cdot T_s]$ |
| Derivative | $K_d \cdot \frac{\mathrm{d}\epsilon(t)}{\mathrm{d}t}$ | $K_d \frac{\epsilon[kT_s] - \epsilon[(k-1)T_s]}{T_s}$ |

Table 5.1: Proportional, integrative, and derivative control action given a control input $\epsilon(t)$

## 5.2 Stator injection method

This section deals with the simulations of all mathematical results coming from Chapter 3, simulating the motor behavior with a MATLAB-Simulink model created with the setup described previously. This section aims to prove that the idea behind the sensorless position and speed estimator presented in [10] is feasible also for applications based on HEMP motors.

### 5.2.1 Observer design validation

The model implemented for the simulations described in this former analysis consists of the simplified motor model. This simplification is achieved by neglecting the presence of magnetic saturation. Under this assumption, the cross-coupling differential inductance $l_{dq}$ is equal to zero. Moreover, the cross-coupling inductance $l_{qe}$ is neglected in a former study, since for the motor construction characteristics, is one order of magnitude lower than the other inductances. These assumptions are based on the theoretical background provided by [11], as already discussed in the former section. Therefore the system is considered linear since the other [l] matrix components are not dependent on the motor working conditions and affect the relation between voltages and currents linearly. First of all Figure 5.2 shows the waveform used for the voltage injection in the simulations. The first simulation procedure is performed by cutting off the motor control d-q-e axis currents and setting the rotor speed to

zero. Under this condition, the only voltage supplied to the motor consists of the high-frequency injection signal.

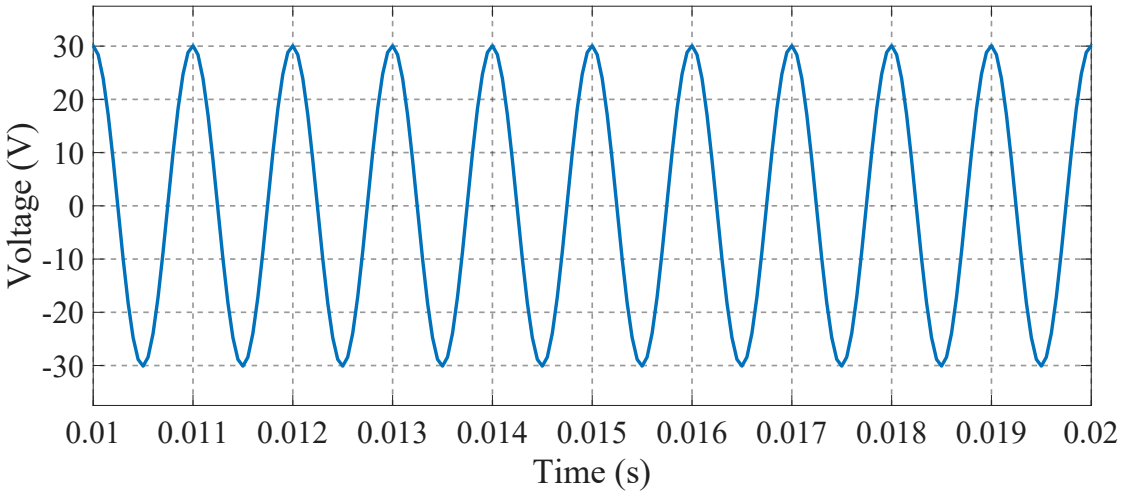


Figure 5.2: Injected voltage waveform for sensorless estimation procedure

This simulation regards the relation between the injected voltage and the induced currents and would be affected by the rotor speed. Figure 5.3 and 5.4 report the simulation behavior of the current propagated by the voltage injection in the direct axis and that one caused by the induced voltage in the excitation winding for different values of reference frame estimation error.

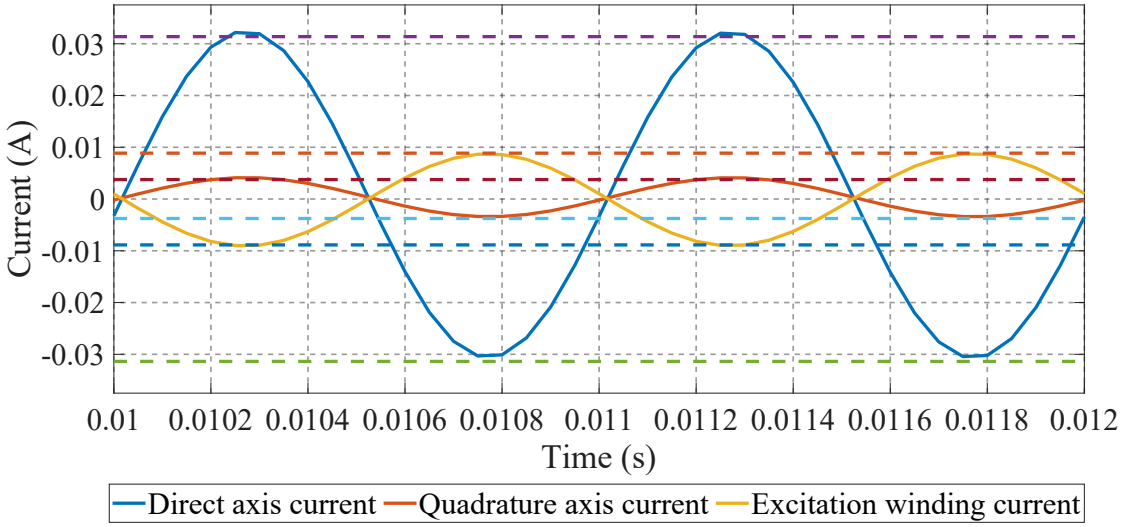


Figure 5.3: Injected currents behaviors for the stator injection estimation method with theoretical boundaries computed in (5.3) for $\Delta\Theta_m^e = \frac{\pi}{8}$ rad

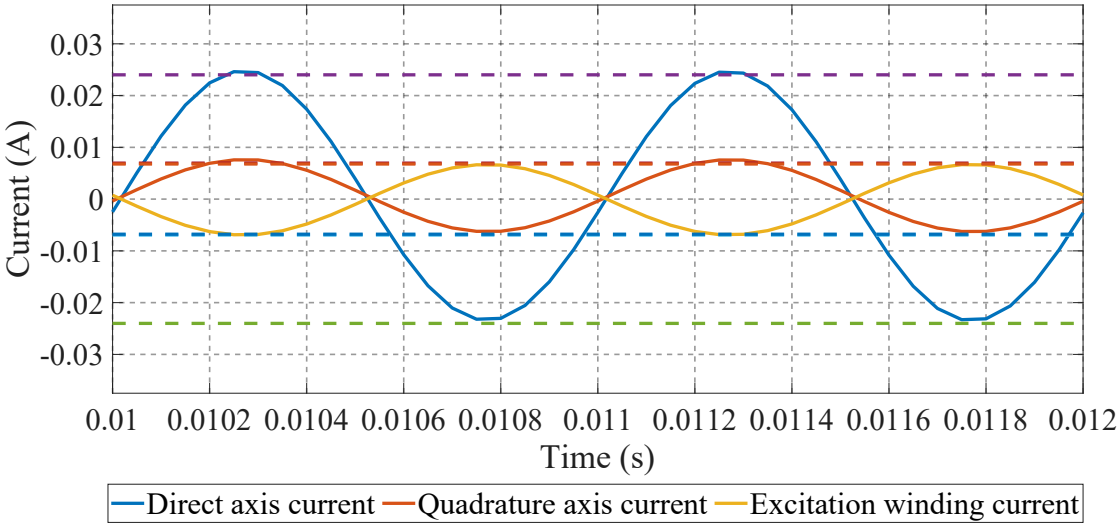


Figure 5.4: Injected currents behaviors for the stator injection estimation method with theoretical boundaries computed in (5.3) for $\Delta\Theta_m^e = \frac{\pi}{4}$ rad

These currents match (5.3), obtained by simplifying (3.7) with the magnetic saturation absence simplification hypothesis.

$$\begin{bmatrix} i_d^{hf}(t) \\ i_q^{hf}(t) \\ i_e^{hf}(t) \end{bmatrix} = \frac{U_{hf} sin(\omega_{hf} t)}{l_{qq} \alpha \omega_{hf}} \begin{bmatrix} 2 l_{qq} l_e cos(\Delta\theta_m^e) \\ (3 l_{de}^2 - 2 l_{dd} l_e) sin(\Delta\theta_m^e) \\ -3 l_{de} l_{qq} cos(\Delta\theta_m^e) \end{bmatrix} \tag{5.3}$$

The next simulation procedure compares the step response of the estimator described in Figure 3.2, with the step response of the closed loop linearized block scheme derived in 3.3. This comparison is shown in Figure 5.5. The observed current behavior matches the signal coming from $W_\theta(s)$ corresponding to the feedback control obtained by negative feedback on the open loop transfer function $G_\theta$. Moreover, the measured rise time is close to the desired one reported in Sec. 3.3. Hence the design strategy is consistent in describing the actual observer behavior. However, an oscillation is present in the true estimator simulation. This behavior is highlighted in Figure 5.6. This figure reports the difference between the theoretical behavior of the high-frequency q-axis current and the outcome of the estimator implemented in the Simulink model. The represented signal corresponds to the waveform with an angular speed of $2w_{hf}$ described in (3.15). This statement is also noticeable from the Fourier transform of the estimated high-frequency q-axis current, shown in Figure 5.19. The frequency behavior of the oscillation matches indeed the sine

wave Fourier transform.

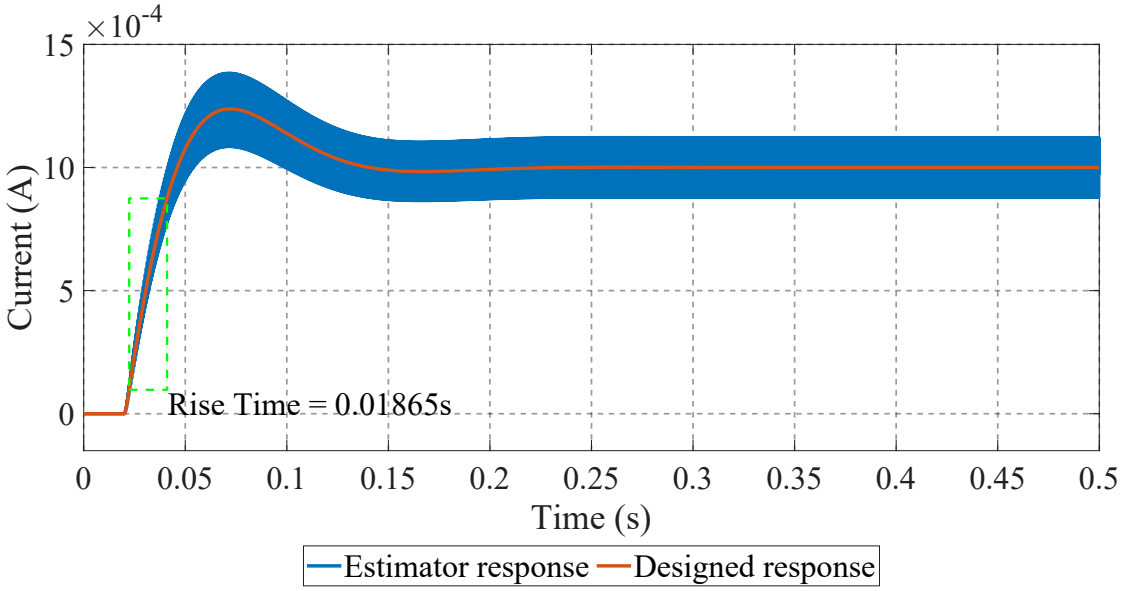


Figure 5.5: Comparison between the simulated $\hat{I}_q^{hf}(s)$ and the simplified transfer function $G_\theta(s)$ for the stator injection method

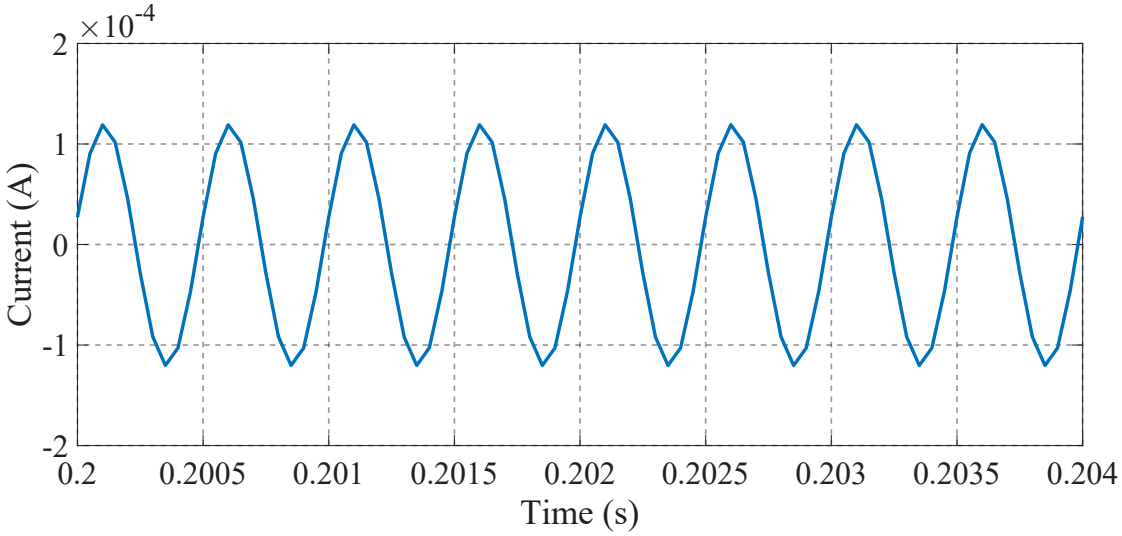


Figure 5.6: Error introduced by the simplification in the controller design for the stator injection method

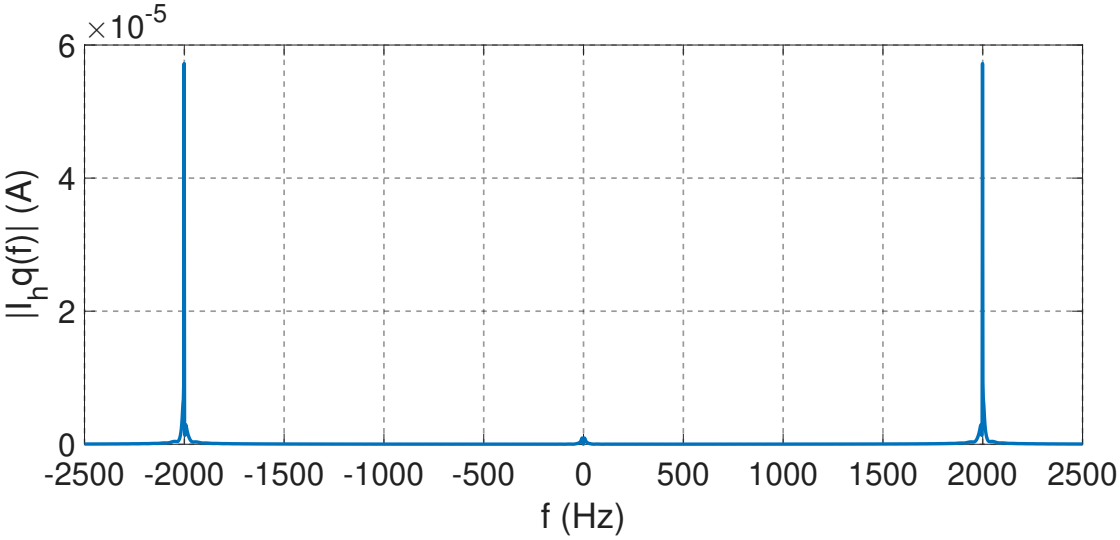


Figure 5.7: Fourier transform of the demodulated q-axis high-frequency error component for the stator injection method

This unexpected behavior is likely due to the low pass filter applied to the demodulated q-axis current which is not ideal and cannot remove completely the high-frequency component of the signal.

### 5.2.2 Zero-speed and low-speed rotor position reconstruction

Also for this simulation procedure, any current control action is disabled. The rotor position changes, simulating a drag by external forces, similar to having the HEPM motor driven by an auxiliary motor. The observer is supposed to guess the correct position. First of all, the motor is set with an initial position different from zero. This experiment aims to see if the initial estimated position $\hat{\theta}_m^e$ converges to the real position $\theta_m^e$ without turning the rotor. This operation is also called zero-speed position estimation. The results of this simulation are reported in Figure 5.8 and in Figure 5.9, respectively the estimated position and the speed behavior with respect to the true rotor position and speed. Both estimations eventually converge to the real values. Moreover, the position step response rise time is comparable to the desired one. The last simulation aims to prove the reconstruction properties of the rotor in movement. Hence in this validation procedure, the low-speed reconstruction capabilities of the estimator are presented. In Figure 5.10 and 5.11 are shown respectively the rotor position and speed estimation with respect to the true values.

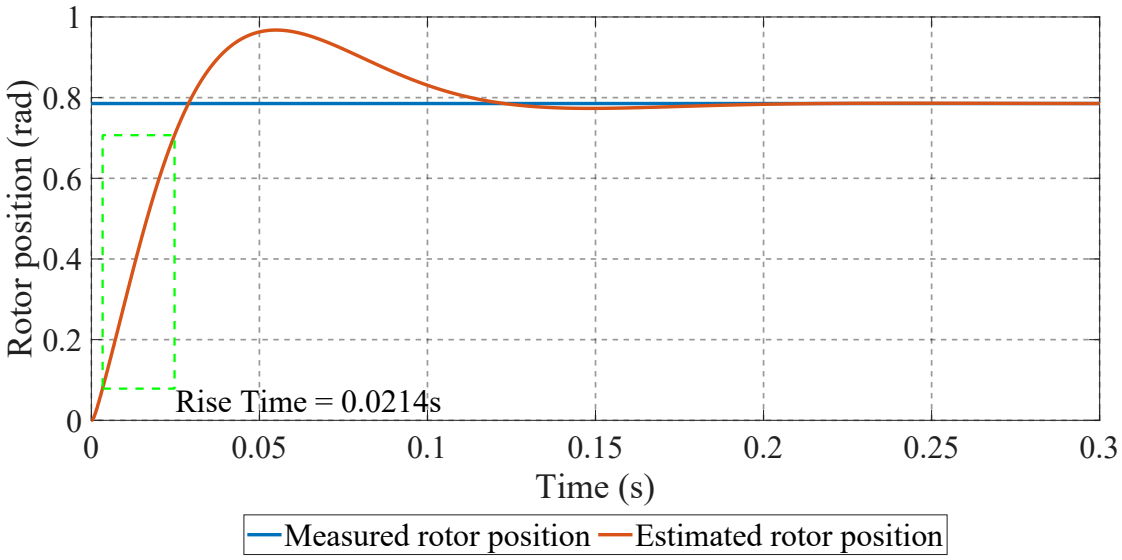


Figure 5.8: Zero-speed rotor position estimation starting from the rotor position $\theta_m^e = \frac{\pi}{4}$ for the stator injection method

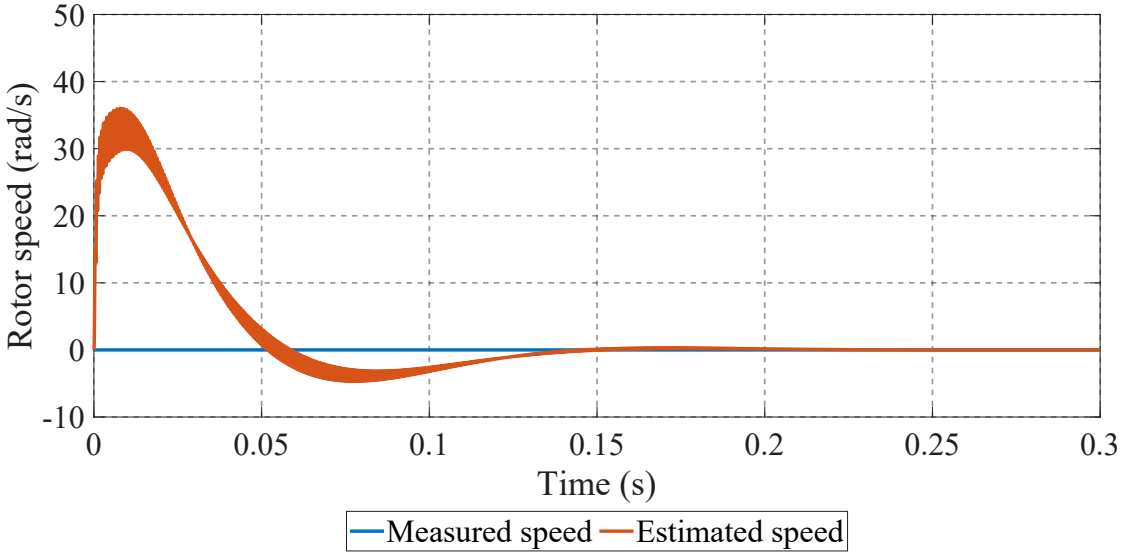


Figure 5.9: Zero-speed rotor speed estimation starting from the rotor position $\theta_m^e = \frac{\pi}{4}$ rads for the stator injection method

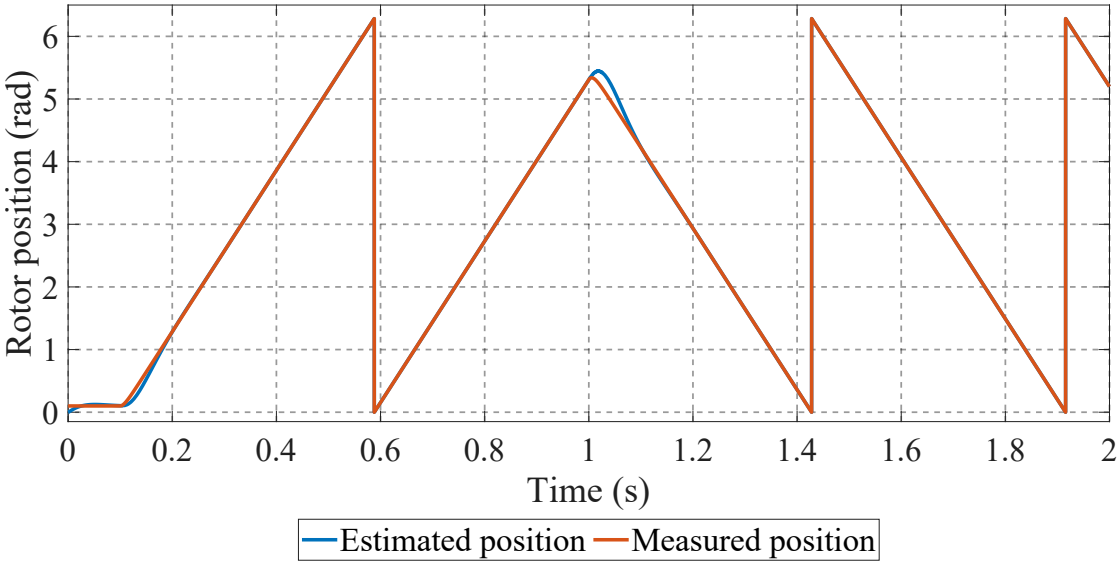


Figure 5.10: Stator injection low-speed rotor position estimation

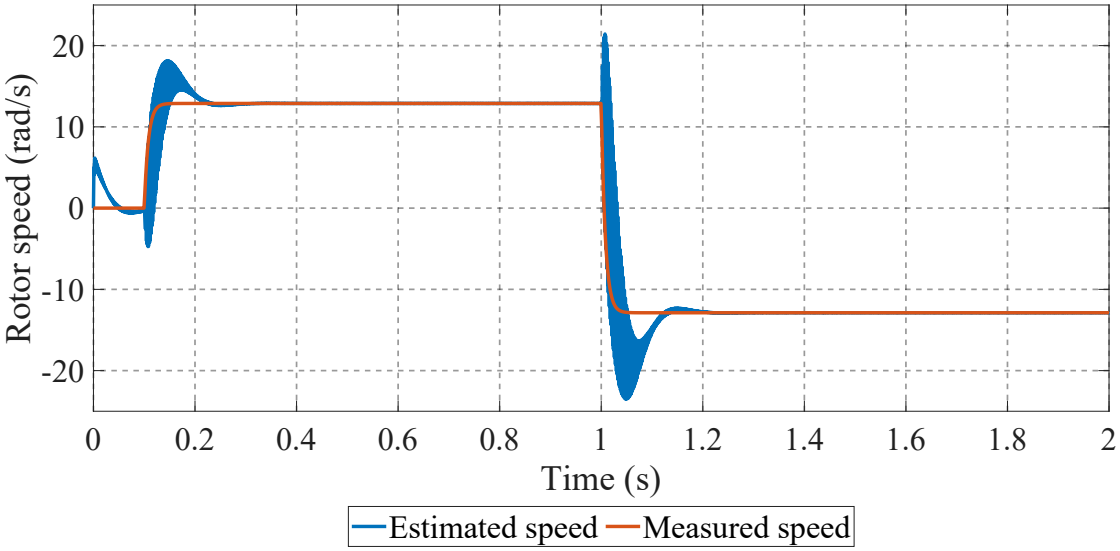


Figure 5.11: Stator injection low-speed rotor speed estimation

### 5.2.3 Magnetic saturation considered

The magnetic saturation effect is now considered. Since this behavior introduces non-linearities in the motor, the motor is modeled thanks to the linearization of the [l] matrix around the machine's working point. This linearization is performed around the values of the excitation current $i_e(t)$ and the motor current derived from the park transform, $i_q(t)$ and $i_d(t)$. This means, as reported in [15], that the cross-coupling differential inductance $l_{dq}$ is no longer zero. This

produces an estimation error which is discussed in this section. Moreover, also the cross-coupling differential inductance $l_{qe}$ is considered different from zero even though this cross-inductance does not numerically affect the estimation that much. Hence to obtain the most accurate error guess, this reconstruction error is analytically derived. For the stator injection method, zeroing (3.12) leads to equation (5.4).

$$\begin{aligned} &\frac{sin(2\Delta\theta_m^e)}{cos(2\Delta\theta_m^e)} = tan(2\Delta\theta_m^e) = \frac{2l_{dq}l_e - 3l_{de}l_{qe}}{\frac{3}{2}\left(l_{de}^2 - l_{qe}^2\right) - l_e\left(l_{dd} - l_{qq}\right)} \\ &\Rightarrow \Delta\theta_m^e = \frac{1}{2}\cdot tan^{-1}\left(\frac{2l_{dq}l_e - 3l_{de}l_{qe}}{\frac{3}{2}\left(l_{de}^2 - l_{qe}^2\right) - l_e\left(l_{dd} - l_{qq}\right)}\right) \end{aligned} \tag{5.4}$$

Figure 5.12 reports the behavior of the position obtained by driving the rotor shaft at a constant speed. As for the former simulation, the driving speed is 5 rad/s, close to the 5% of the motor base speed. In this figure the shifting between the true and the estimated position is visible. This time shift is caused by the embedded estimation introduced by the nonlinearities described earlier. This error follows (5.4), as reported in Figure 5.13 where the error computed analytically matches asymptotically the error defined as the difference between the reconstructed and the measured position.

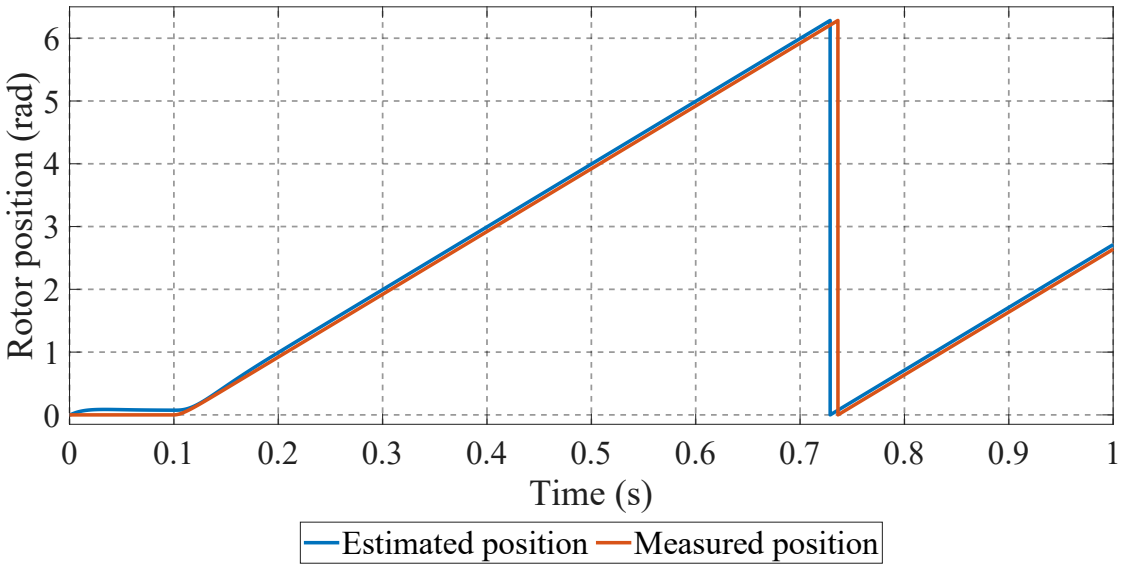


Figure 5.12: Estimated rotor position from the stator injection-based observer in comparison with the measured rotor position

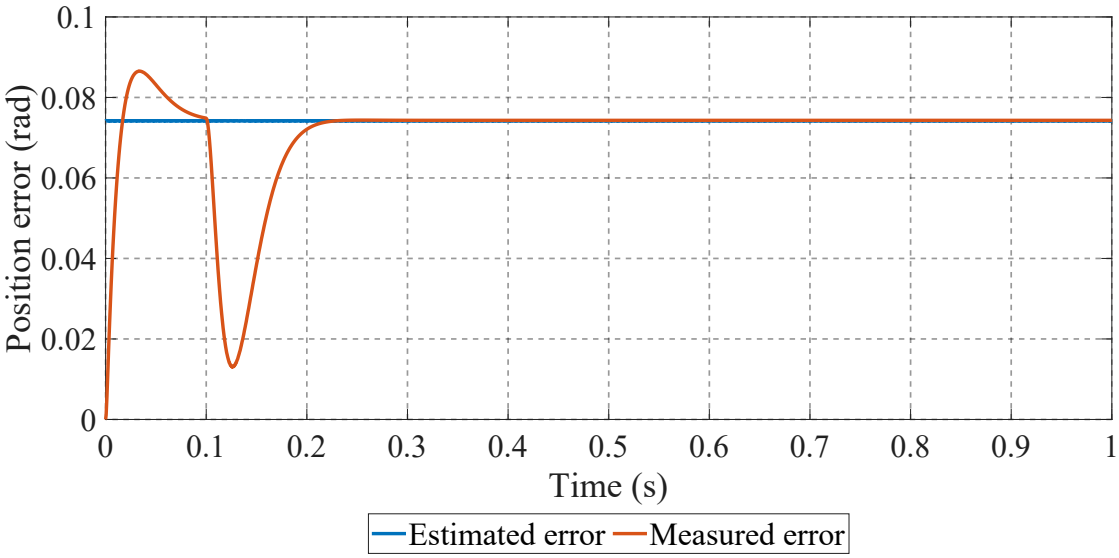


Figure 5.13: Predicted rotor position reconstruction error in comparison with actual estimation error coming from the stator injection-based observer

## 5.3 Rotor injection method

This section presents the validation through the mathematical model for the results discussed in chapter 4. This validation is performed thanks to the Simulink model described in Sec. 5.1.

### 5.3.1 Observer design validation

As during the stator injection method numerical validation, the first test has been performed with rotor mechanical speed zero and no control action on the d-q-e axis current controller. The first main difference is noticeable in Figure 5.14, where the d-axis current is different from zero. This behavior is shown in detail in Figure 5.15 and is explained by the equation (2.2). Remembering that in the simulation performed the motor rotor is stopped ($\omega_m^e = 0$) and, for equation (4.1), the d-axis current derivate is equal to zero, the equation perfectly matches the voltage behavior. Figure 5.15 is also reporting the maximum and minimum values computed from equation (5.5).

$$u_d^{hf}(t) = R_s i_d^{hf}(t) = \frac{2R_s U_{hf} L_{de}}{\omega_{hf}\alpha} \cdot sin(\omega_{hf}(t)) \tag{5.5}$$

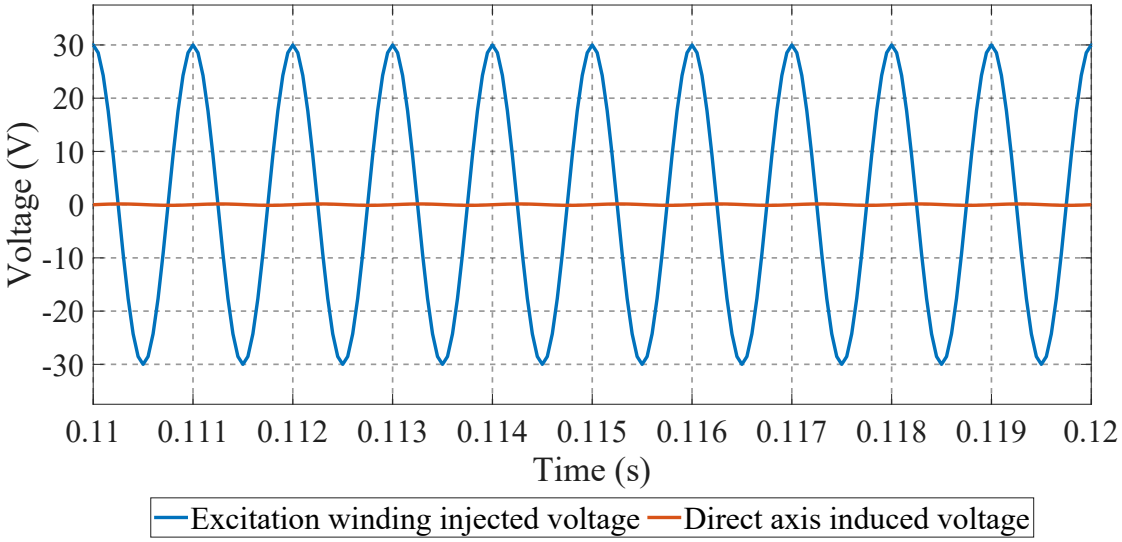


Figure 5.14: Excitation winding injected voltage and induced voltage in the d-axis

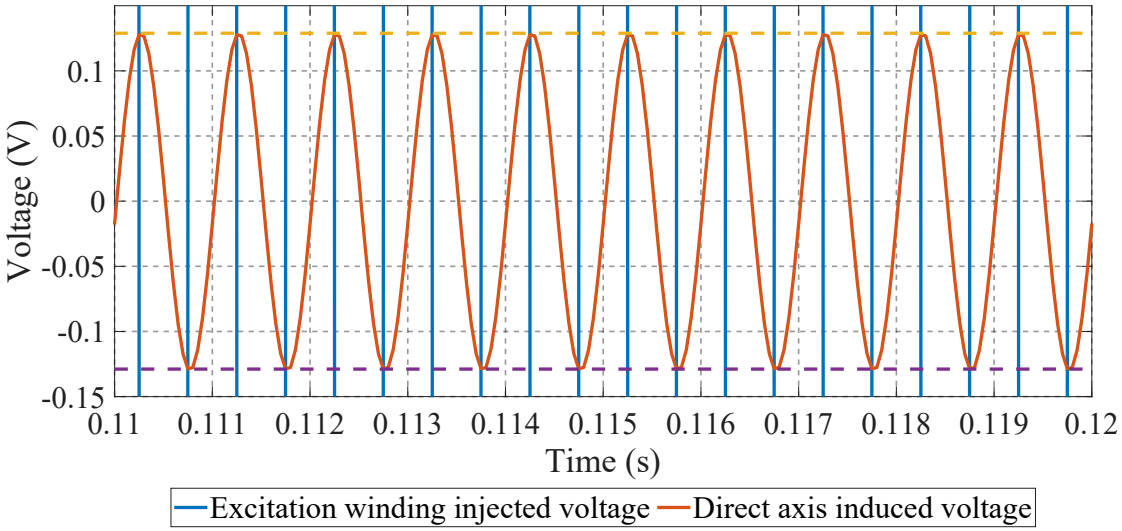


Figure 5.15: Detail of the voltage in the d-axis induced by the injected voltage

Figure 5.16 reports the current propagated in the excitation winding and in the true direct axis since the model is simulated with the rotor in a stand-still state ($\theta_m^e = 0$). This figure also shows the maximum and minimum values for the sinusoidal waveform exploited in (5.6). These limits correspond to the simplification of (4.2) substituting $l_{dq}$ and $l_{qe}$ with zero due to the magnetic saturation absence hypothesis.

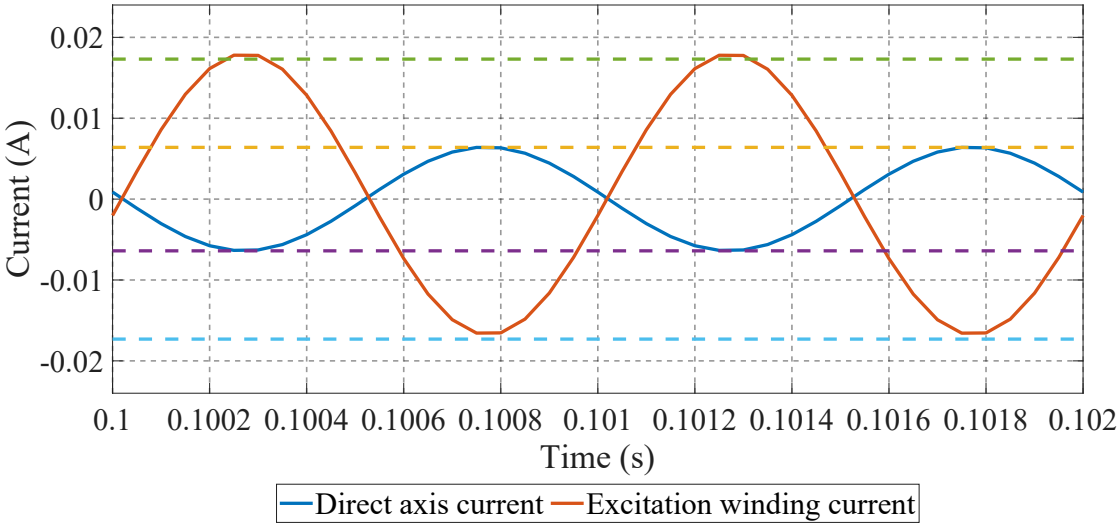


Figure 5.16: Injected currents behaviors with theoretical boundaries for rotor injection method

$$\begin{bmatrix} i_d^{hf}(t) \\ i_q^{hf}(t) \\ i_e^{hf}(t) \end{bmatrix} = \frac{U_{hf} sin(\omega_{hf} t)}{\alpha \omega_{hf}} \cdot \begin{bmatrix} -2l_{de} \\ 0 \\ 2l_{dd} \end{bmatrix} \tag{5.6}$$

As already exploited in Sec. 5.2.1, the next validation step consists of the comparison between the actual estimator demodulation response, described in Figure 3.2, and the linearized transfer function obtained in (4.7). In Figure 5.17 is reported the true estimator response, compared with the response coming from the controlled transfer function, described in Figure 3.3. Figure 5.18 reports in detail the difference between the estimated and the simulation currents. It is noticeable that the behavior of the current coming from the estimator matches the signal coming from the transfer function used for the controller computation. Hence the design strategy is consistent in describing the actual observer behavior also for the rotor injection method. Figure 5.19 shows the Fourier transform performed on the estimated high-frequency q-axis current. This current, displayed in Figure 5.17 and Figure 5.18, is coming from the simulation. It is noticeable that the signal presents the same behavior as described in Sec. 5.2.1. Moreover, the step response outcome on this validation test is the same for both estimation methods. This proves that the controller design is consistent for both observers.

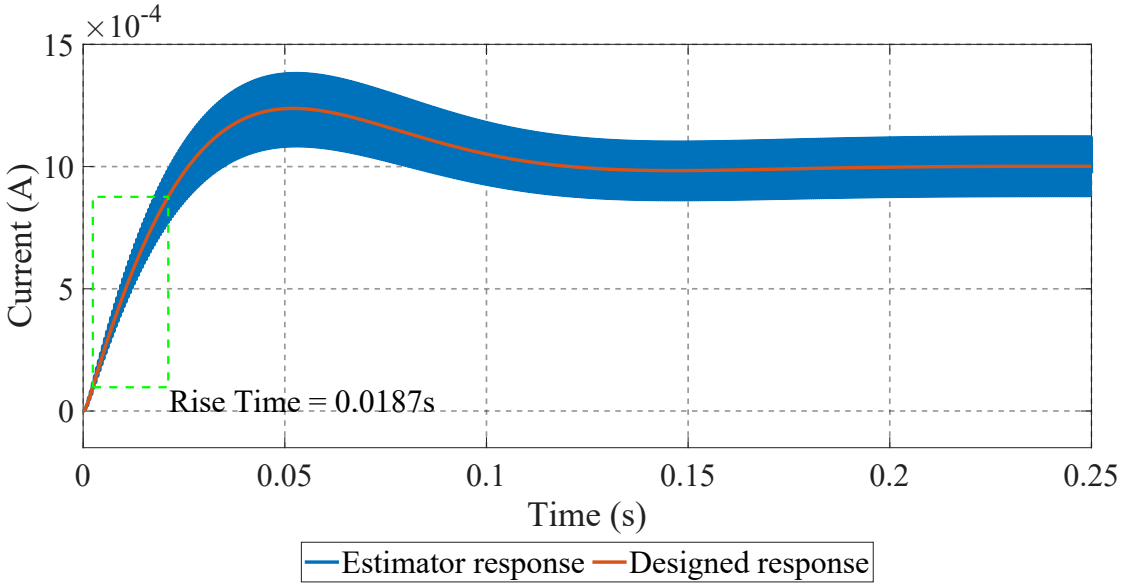


Figure 5.17: Comparison between the seimulatad $\hat{I}_q^{hf}(s)$ and the simplified transfer function $G_\theta(s)$ for the rotor injection method

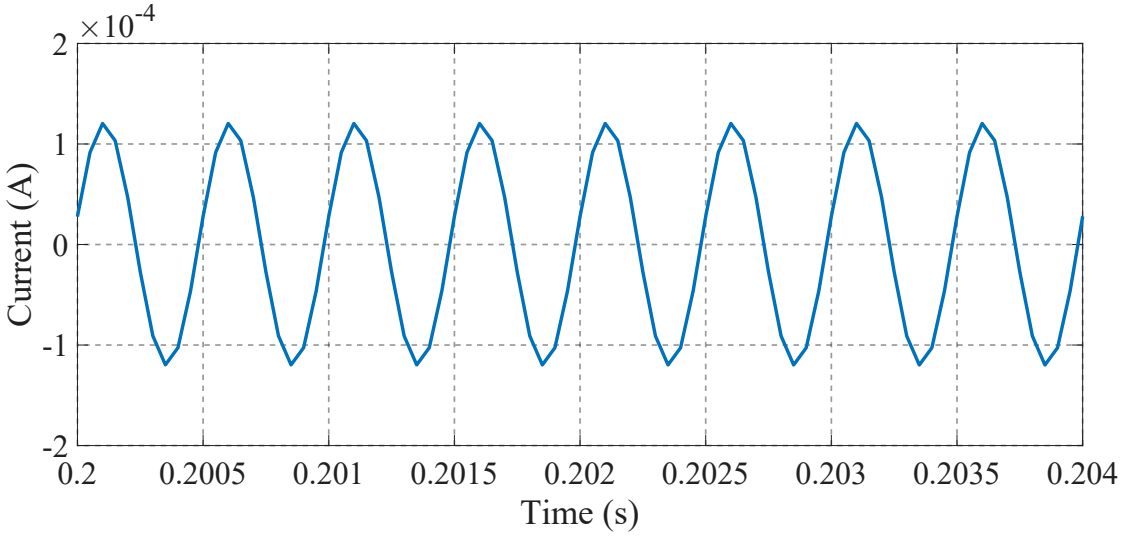


Figure 5.18: Error introduced by the simplification in the controller design for the rotor injection method

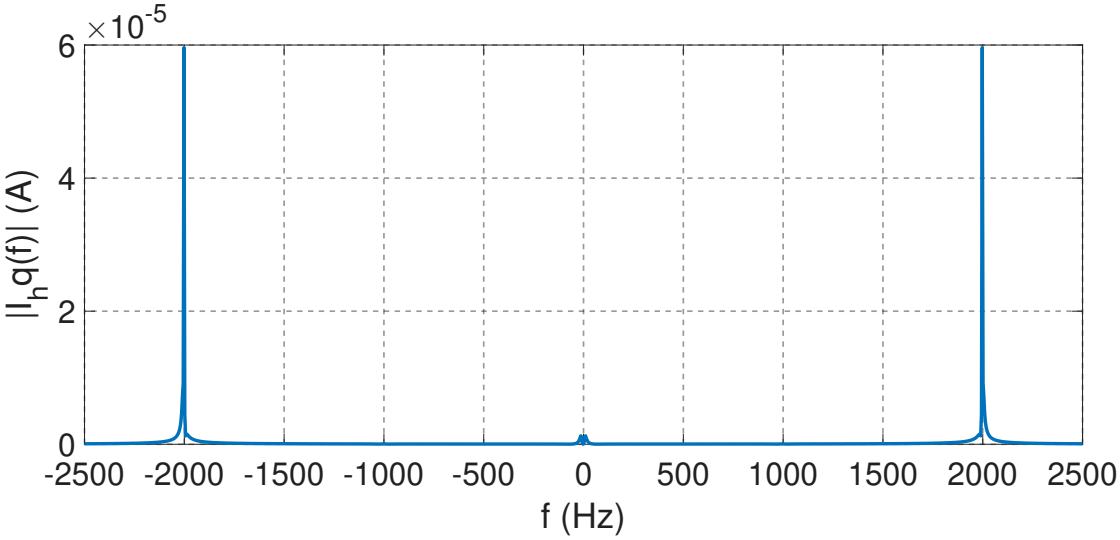


Figure 5.19: Fourier transform of the demodulated q-axis high-frequency error component for the rotor injection method

### 5.3.2 Zero-speed and low-speed rotor position reconstruction

As in Sec. 5.2.2, any motor current control action is disabled, with the rotor position free to change. In Figure 5.20 and in Figure 5.21, is reported respectively the estimated position and the estimated speed behavior with respect to the true rotor position and speed, starting from an initial rotor position of $\frac{\pi}{4} rad$.

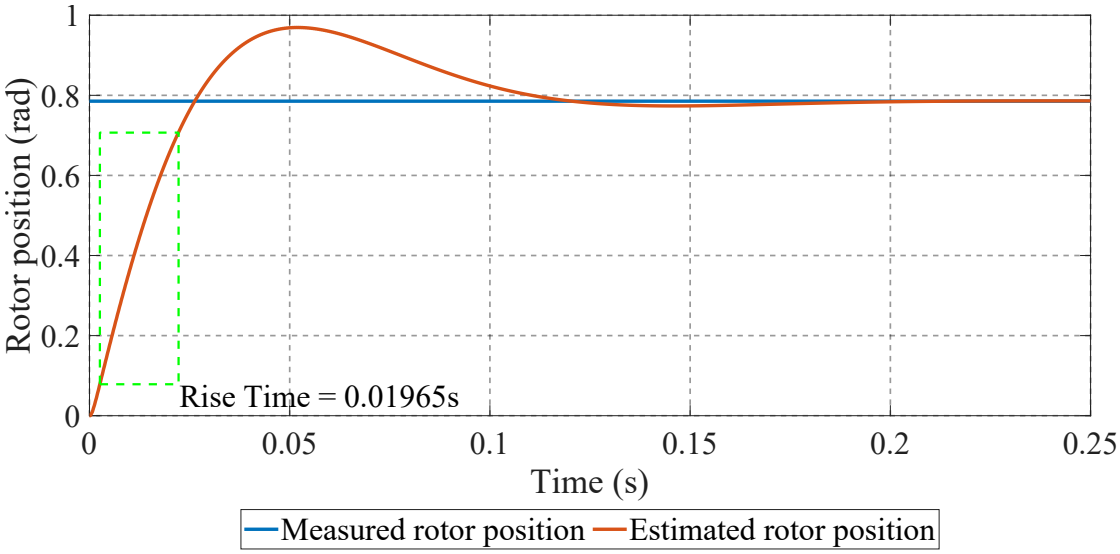


Figure 5.20: Zero-speed rotor position estimation starting from the rotor position $\theta_m^e = \frac{\pi}{4}$ for the rotor injection method

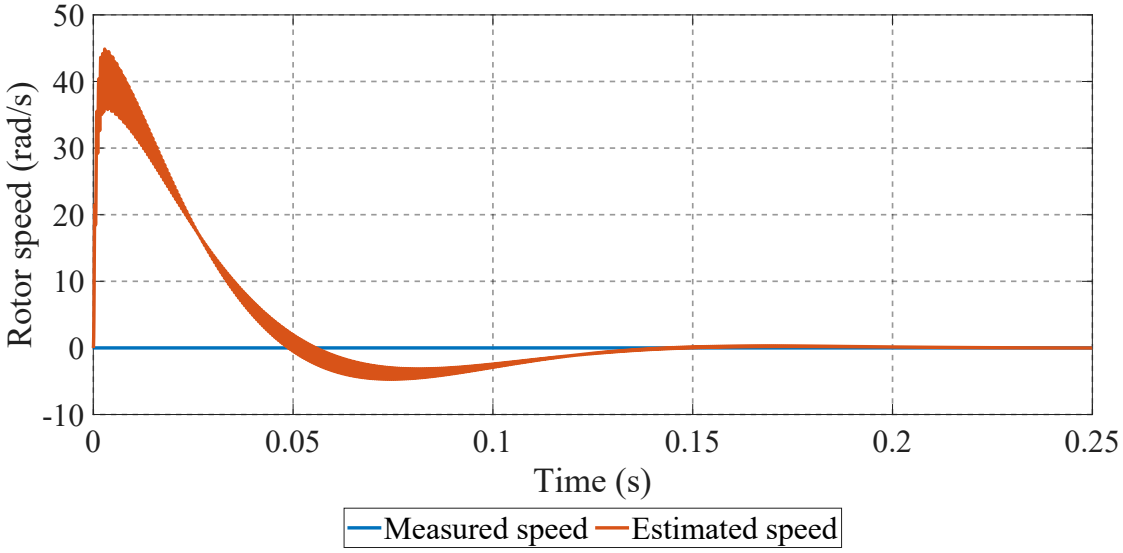


Figure 5.21: Zero-speed rotor speed estimation starting from the rotor position $\theta_m^e = \frac{\pi}{4}$ for the rotor injection method

As for the stator injection method, at steady state, both estimations converge to the true values. Moreover, the step response rise time of the rotor position estimation is comparable to the designed one. This validates the zero-speed estimation capabilities for the rotor injection observer. In the last simulation, Figure 5.10 and 5.11 showed respectively the rotor position and speed estimation for the rotor rotating at low speed. Therefore the low-speed estimation capabilities have been validated.

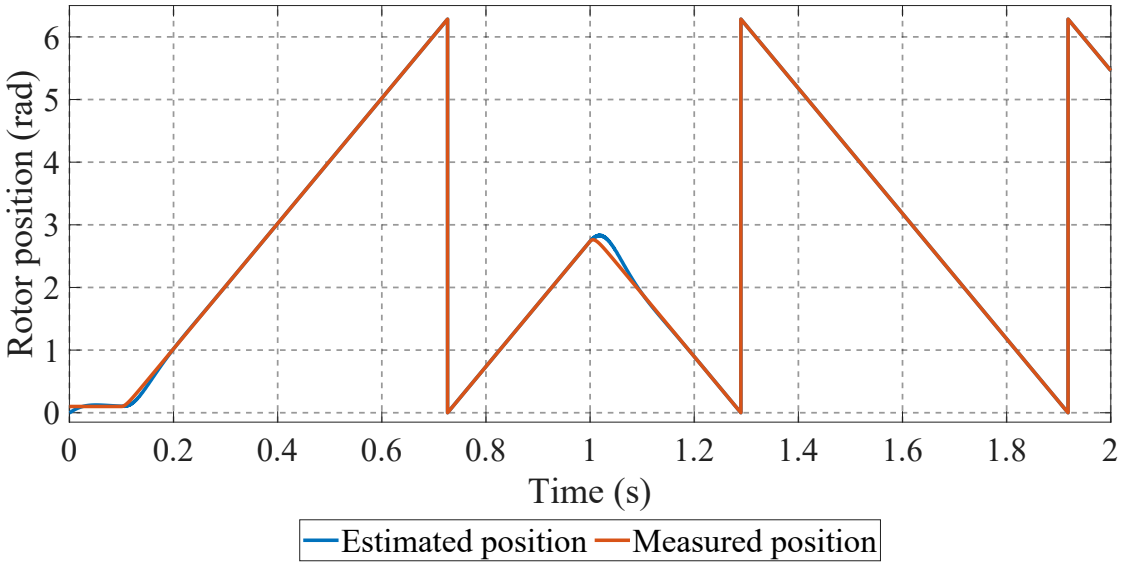


Figure 5.22: Rotor injection observer low-speed rotor position estimation

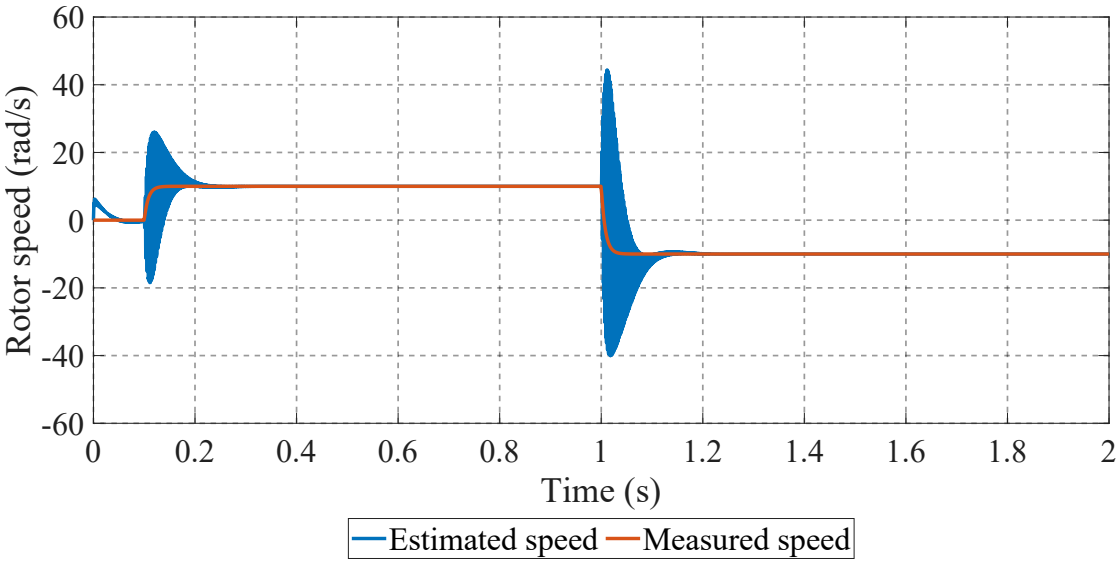


Figure 5.23: Rotor injection observer low-speed rotor speed estimation

### 5.3.3 Magnetic saturation considered

As already described in Sec. 5.2.3 the cross-coupling magnetic saturation is considered also for the high-frequency rotor injection estimation method. The analytical derivation of the position reconstruction error caused by the mutual cross differential inductances $l_{dq}$ and $l_{qe}$ is derived zeroing the q-axis current component in (4.3). This component is directly connected to the observer error. In (5.7) is presented the analytical derivation for the estimation error.

$$\begin{aligned} \frac{sin(\Delta\theta_m^e)}{cos(\Delta\theta_m^e)} = tan(\Delta\theta_m^e) = \frac{l_{de}l_{dq} - l_{dd}l_{qe}}{l_{de}l_{qq} - l_{dq}l_{qe}} \\ \Rightarrow \Delta\theta_m^e = tan^{-1}\left(\frac{l_{de}l_{dq} - l_{dd}l_{qe}}{l_{de}l_{qq} - l_{dq}l_{qe}}\right) \end{aligned} \tag{5.7}$$

Figure 5.24 shows the estimated position derived by rotating the motor shaft at the constant speed of 5 rad/s. There is a noticeable shift between the measured and the estimated position. This behavior is the same as for the stator injection estimation method but comes with a different position reconstruction error. This error asymptotically converges to the theoretical error computed with (5.7), as shown in Figure 5.25.

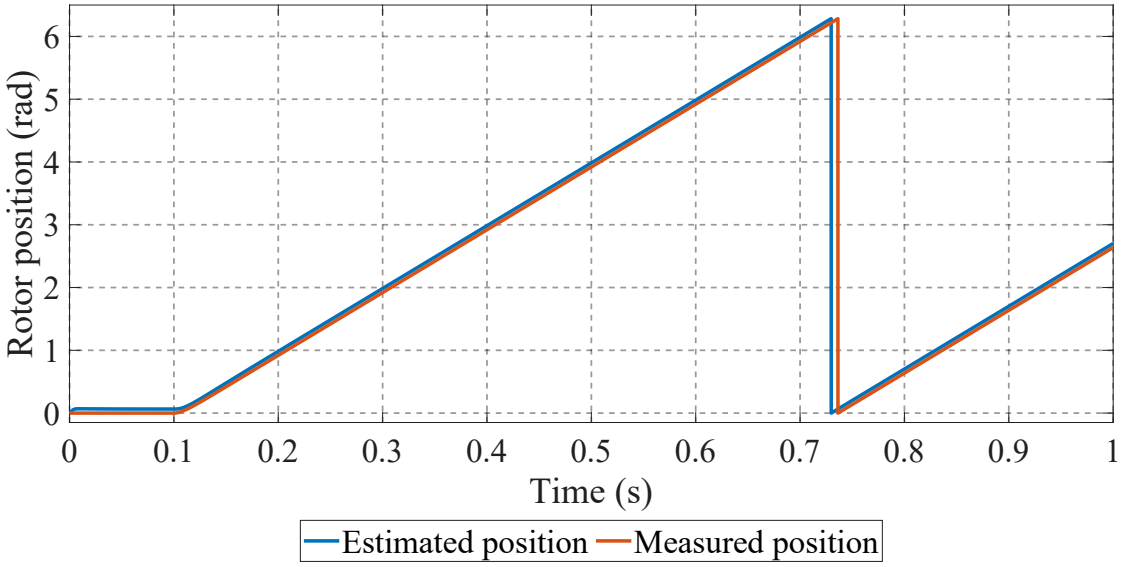


Figure 5.24: Estimated rotor position from the rotor injection-based observer in comparison with the measured rotor position

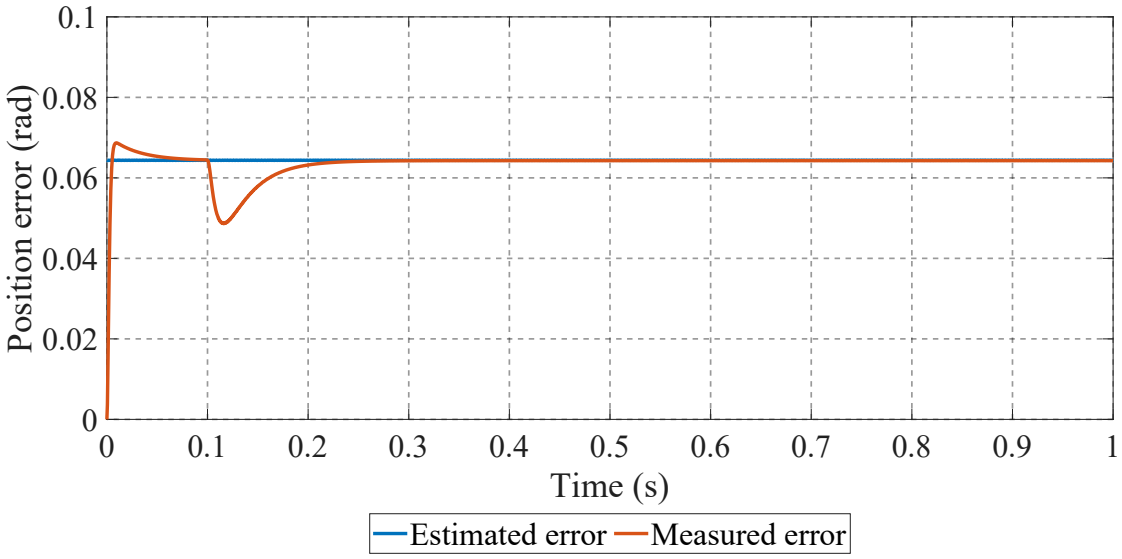


Figure 5.25: Predicted rotor position reconstruction error in comparison with actual estimation error coming from the rotor injection-based observer

# 6

# Estimated Speed Feedback Control Design

In this chapter, the design for the speed control with estimated speed and position feedback is discussed. First of all, the project requirements for the speed dynamics are:

- Cut-off frequency $\omega_{gc} = 10\pi\ rad/s$, corresponding to a f = 5 Hz control band with;
- Phase margin $\phi = 60°$;

In order to obtain the project requirements for speed control, the behavior of the filtering action of the speed and position observer must be taken into account in the controller design process.

## 6.1 Measure filter derivation

To get the actual transfer function describing the relation between the true and the estimated speed, we start analyzing the scheme provided in Figure 3.3. After some block algebra expressing $\Theta_m^e(s)$ as input, Figure 6.1 is derived from the block scheme describing the relation between the measured position and the estimated one. First of all, the q-axis current $I_q^*(s)$ is zero since is the reference for that current. In equation (6.1) is presented the transfer function between the measured and the estimated position.

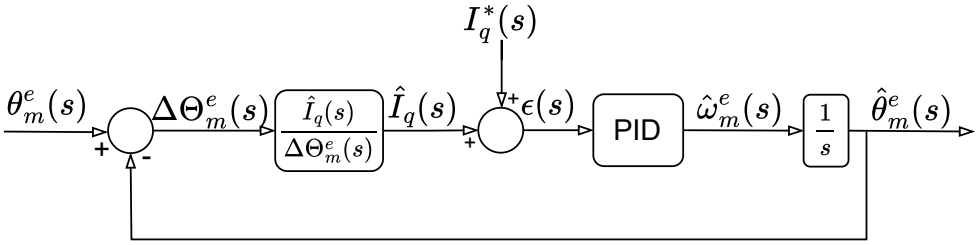


Figure 6.1: Block diagram of the measure-to-estimated position transfer function

$$W_{\hat{\theta}}(s) = \frac{\hat{\Theta}_m^e(s)}{\Theta_m^e(s)} = \frac{PI_{\hat{\omega}(s)} \cdot G_\theta(s)}{1 + PI_{\hat{\omega}(s)} \cdot G_\theta(s)} = \frac{\tilde{G}(s)}{1 + \tilde{G}(s)} \tag{6.1}$$

$\tilde{G}(s)$ is the open loop compensated transfer function between the Park transform reference frame error and the q-axis current. Moreover, while $G_{\hat{\theta}}(s)$ depends on the injection method, thanks to the normalization step in the estimator PI design, both injection methods lead to the same compensated transfer function. This means that also the measured-to-estimated position function is the same among the two observers. Since the electro-mechanical position corresponds to the integration over time of the electro-mechanical speed, also the speed relation is the same as the position one. Hence for the Laplace transform perspective, the derivation operation consists of multiplying by the $s$ factor. This multiplication is performed on both numerator and denominator of the $W_{\hat{\theta}}(s)$ transfer function, leading to (6.2). Moreover, since the electro-mechanical speed is computed by multiplying the mechanical rotor speed for the motor pole pairs, $W_{\hat{\omega}}$ is also the measured-to-observed mechanical speed transfer function.

$$W_{\hat{\omega}}(s) = \frac{\hat{\Omega}_m^e(s)}{\Omega_m^e(s)} = \frac{\not{s}\hat{\Theta}_m^e(s)}{\not{s}\Theta_m^e(s)} = W_{\hat{\theta}}(s) = \frac{\tilde{G}(s)}{1 + \tilde{G}(s)} \tag{6.2}$$

On the other hand, the observed speed estimations present some differences among the two methods, even though the observed position keeps the same behavior. This phenomenon, also noticeable in Sec. 5.2.1 and Sec 5.3.1, is likely due to the component that the low-pass filter is not able to cancel. This occurs because of the non-idealities characterizing the filters. This component is amplified by the PI controllers inside the speed and position observer, causing different behavior due to the observers' differences. However, the position estimation gets a filtering action from the observer control structure thanks to the integral action. Therefore, the speed presents oscillation that must be filtered to

use the observed speed as the feedback measure for the speed control. To remove this oscillation component a second-order Butterworth filter is introduced. Its transfer function is described in (6.3) where $\omega_{bu}$ is the cut-off frequency of the Butterworth low pass filter. For this case of study, the filter cut-off frequency is an order of magnitude higher than the speed control bandwidth (50Hz).

$$LPF_2(s) = \frac{\omega_{bu}^2}{s^2 + \xi\omega_{bu}s + \omega_{bu}^2} \tag{6.3}$$

## 6.2 Control scheme analysis and PID design

Figure 6.2 presents the speed control scheme implemented for the mechanical speed control.

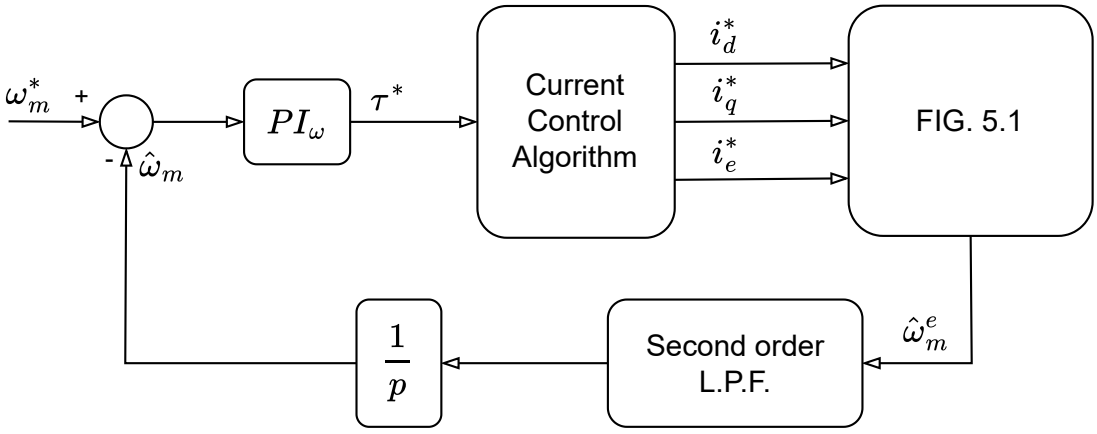


Figure 6.2: Speed feedback control scheme using the estimated speed as the control measure

The MTPA current reference computation has been chosen as the current control strategy for this work. The excitation current is controlled to a constant value, making the torque-to-current mapping function similar to that of a standard IPM motor. This is not the most efficient strategy for setting the current references, but it's reliable and widely used. However other efficient methods can be used as described in [15] without changing the estimation procedure. The motor control currents and the current propagated inside the machine due to the high-frequency injection are operating at different frequencies. Hence the separation performed by the filters makes the rotor speed and position estimation task robust to any current control strategy. To get the transfer function that

can be used to derive the speed controller design, it is helpful to make a couple of simplifications. First of all, the current dynamics are two orders of magnitude higher than the desired control bandwidth for the speed controller. Hence the transient dynamics for the d-q axis current can be neglected considering the current reference values to be always applied on the motor. However, the current references are computed thanks to the MTPA algorithm while the torque generated from the motor currents follows the torque equation used for the MTPA reference generation. Hence, from the perspective of the speed control dynamics, the reference torque is directly applied to the motor shaft. Moreover, the transfer function from the torque to the rotational speed of a motor shaft is reported in (6.4) where B and J are respectively the friction coefficient and the rotational inertia of the motor shaft.

$$\Gamma(s) = \frac{\Omega(s)}{\mathrm{T}(s)} = \frac{1}{1 + \frac{J}{B}s} \tag{6.4}$$

The control scheme is then represented in Figure 6.3.

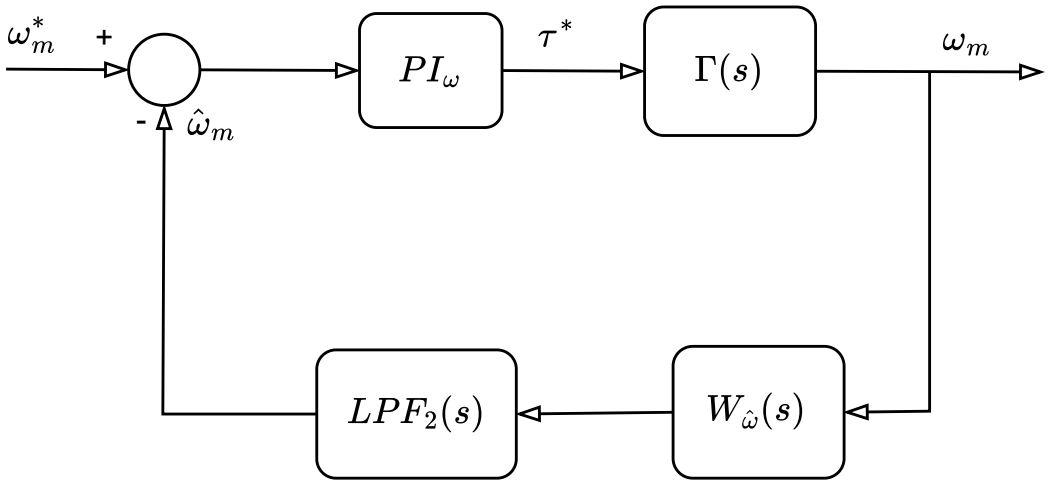


Figure 6.3: Speed feedback equivalent block scheme

This scheme is characterized by the comprehensive transfer function described in (6.5). The poles of this function describe the speed dynamics. The PID controller structure is introduced since is the canonical control strategy that gives better results among all the tested designs. The controller coefficients have been computed, like all the other controllers in this work, thanks to the Matlab

Control System Toolbox.

$$W_\omega(s) = \frac{PI(s)\Gamma(s)}{1 + PI(s)\Gamma(s)W_{\hat{\omega}}(s)LPF_2(s)} \tag{6.5}$$

# 7

# Method Comparison

Follows the analysis of the characteristics and the performances of the two estimators. The first comparison, showed in Figure 7.1, concerns the embedded position estimation error discussed in Sec. 5.2.3 and Sec.5.3.3.

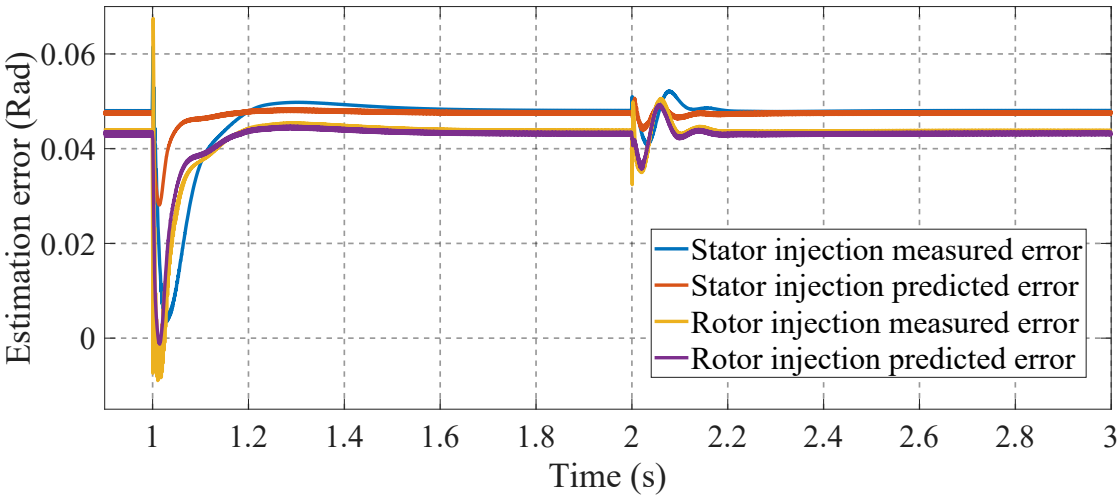


Figure 7.1: Confrontation between the methods measured position reconstruction error and the estimated error coming from the error prediction equations (5.4) and (5.7)

This error, as described respectively in (5.4) and (5.7) is affected by the operating point of the motor, in particular from the current flowing inside both the stator and the rotor. However, in all the setups discussed in this work, the rotor injection method is characterized by a lower error. Although this difference is small, for a task like the position control, the rotor injection method is preferable

since it presents a lower position reconstruction error. Anyway, the correction of the position measure is feasible. As reported in Fig: 7.1, the error coming from the prediction is very close to the actual error introduced by the cross-coupling inductances. Since as reported in Chapter 6 the transfer function characterizing both observed speed-based control methods are the same, follow up only the results for the rotor injection method. The two methods are comparable from the perspective of speed control capabilities. Figure 7.2 presents the measured speed behavior of both estimation methods comparison between the two observer methods when the estimated speed is used as feedback for the speed control.

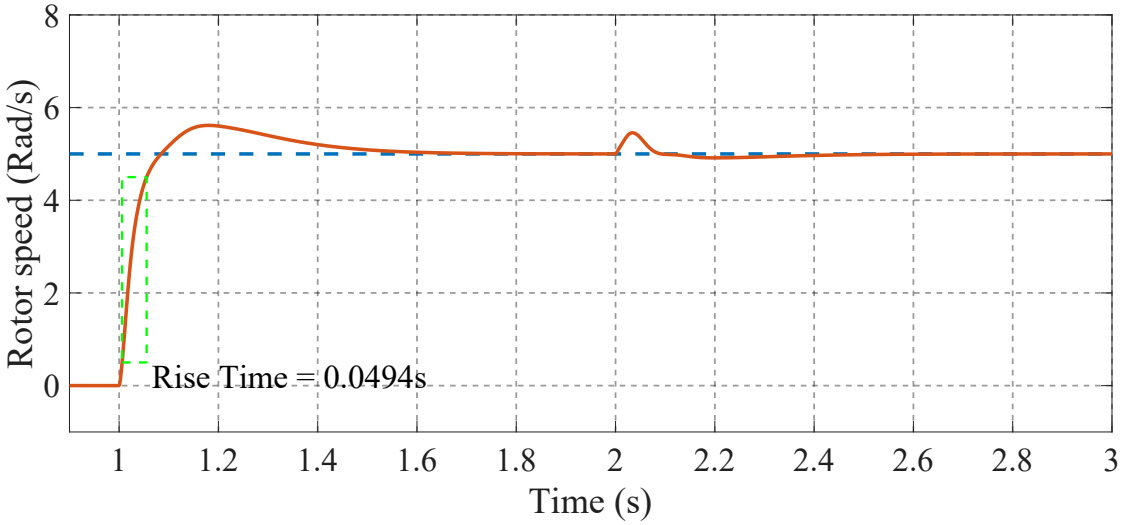


Figure 7.2: Measured speed step response with estimated speed and position feedback controller

The measured speed reaches the reference signal (the dashed line) with a response characterized by rise time corresponding to a control bandwidth of almost 7Hz. This result is acceptable considering the complexity of the control design. Moreover, a constant torque disturbance has been introduced in the control input. The effect of the disturbance is visible at time 2 seconds of Figure 7.2 and proves the robustness of the control method, rejecting the constant actuation disturbances. These results for the speed control have been achieved by performing the reference frame estimation error compensation to the observed position. This grants a precise transformation when applying the inverse Park transform to compute the alpha-beta voltages that the inverter generates. The correction effect is shown in Figure 7.3 where the true and estimated positions have been compared.

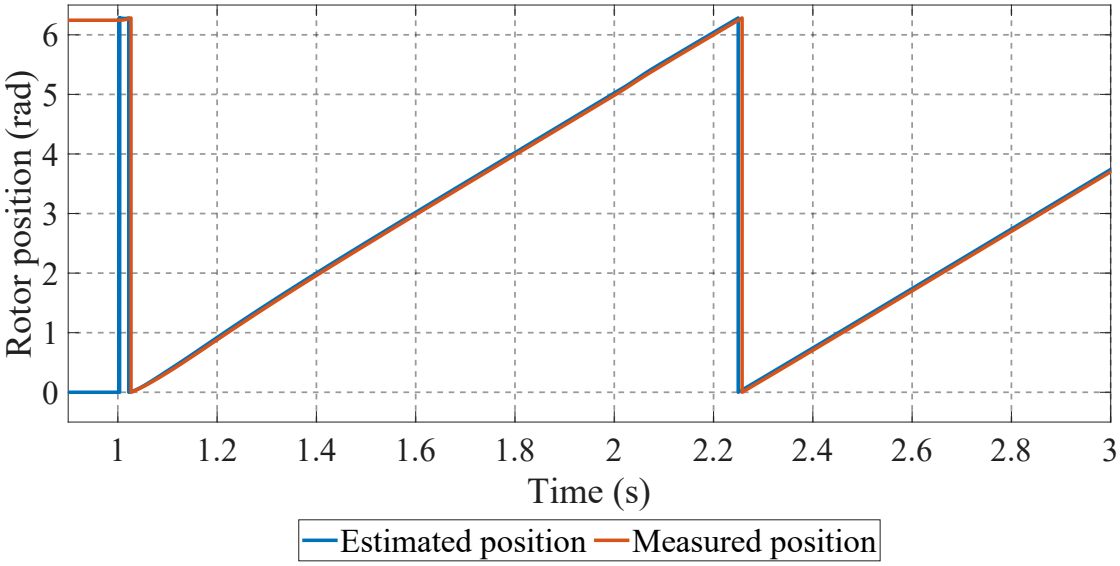


Figure 7.3: Measured versus observed electro-mechanical position after error compensation

The most noticeable difference coming from the confrontation of the two estimation methods is the zero-speed reconstruction capabilities. The initial position reconstruction for the stator injection method is not reliable for every initial position. As shown in Figure 7.4 with the true electro-mechanical position in proximity of $\pi$ is estimating the observer is estimating the wrong angle.

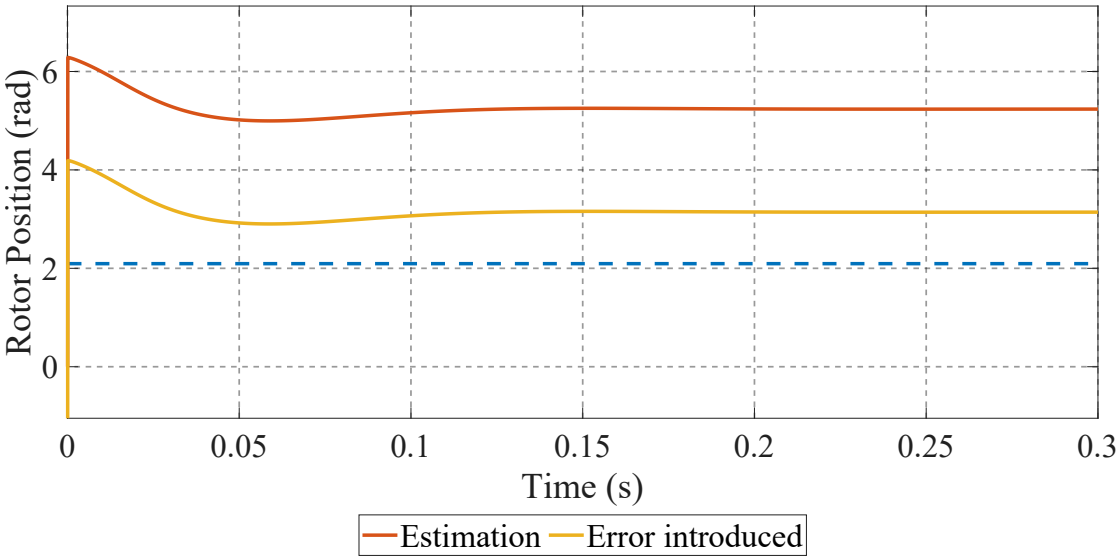


Figure 7.4: True (dashed) versus estimated position with $\Theta_m^e = 2.09$ rad with the estimation error for stator injection method

Therefore the estimation introduces an error of exactly $\pi$ radians. This error

is present in every estimation performed with an initial error $\Delta\Theta_m^e$ greater than $\pi/2$ radians. This behavior is shown in Figure 7.5 which reports the stator injection estimation output with respect to the true rotor position.

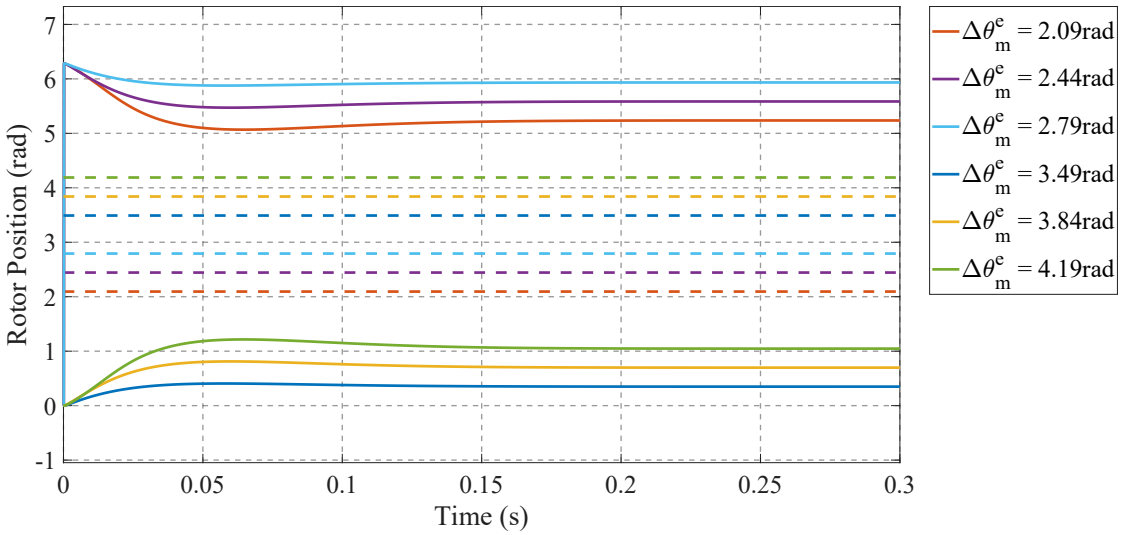


Figure 7.5: Measured (dashed) versus estimated position for zero-speed stator injection estimation method with an initial position in proximity of $\theta_{me} = \pi$

In particular is noticeable that the interval around $\pi$ is mapped in the interval around $2\pi$, that for the angle multiplicity became zero. Figure 7.6 reports the estimated speed generating the position for the stator injection method.

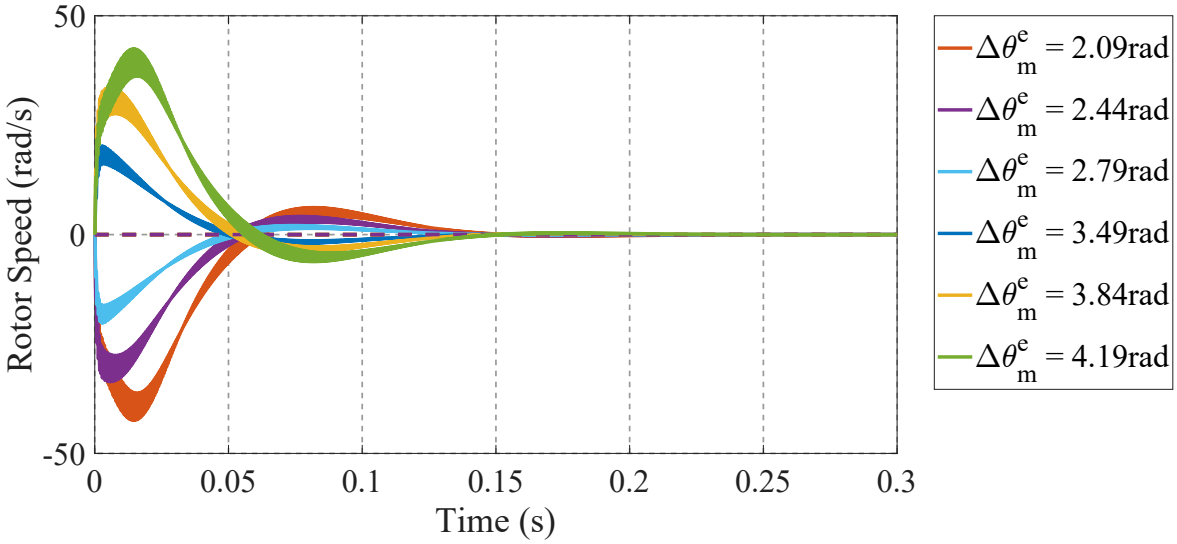


Figure 7.6: Measured (dashed) versus estimated speed for zero-speed stator injection estimation method with an initial position in proximity of $\theta_{me} = \pi$

On the other hand, the rotor injection estimation with an initial electromechanical position around $\pi$ is correct. This is reported in Figure 7.7 with Figure 7.8 describing the estimated speed generating the position reconstruction.

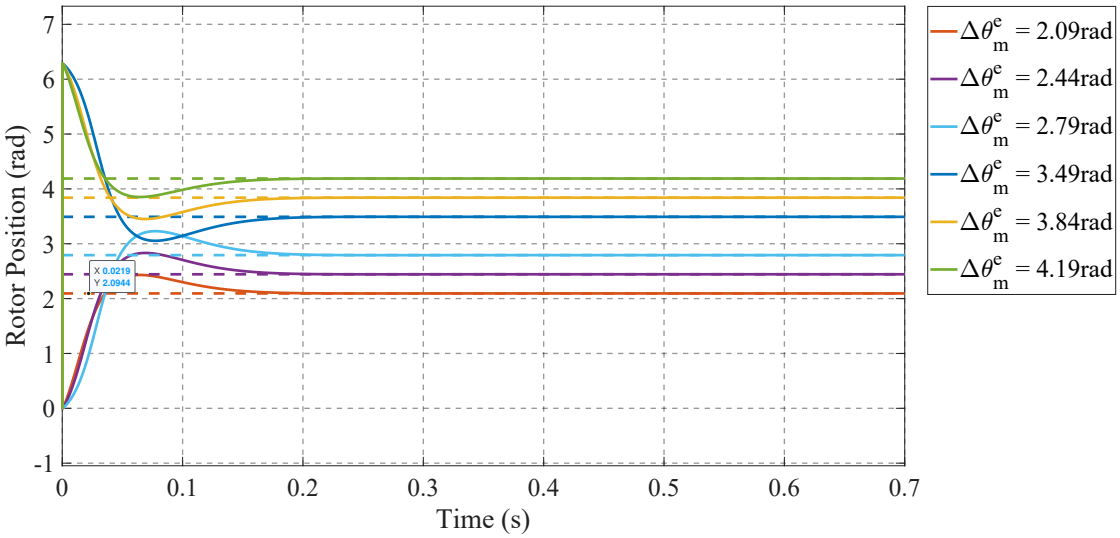


Figure 7.7: Measured (dashed) versus estimated position for zero-speed rotor injection estimation method with an initial position in proximity of $\theta_{me} = \pi$

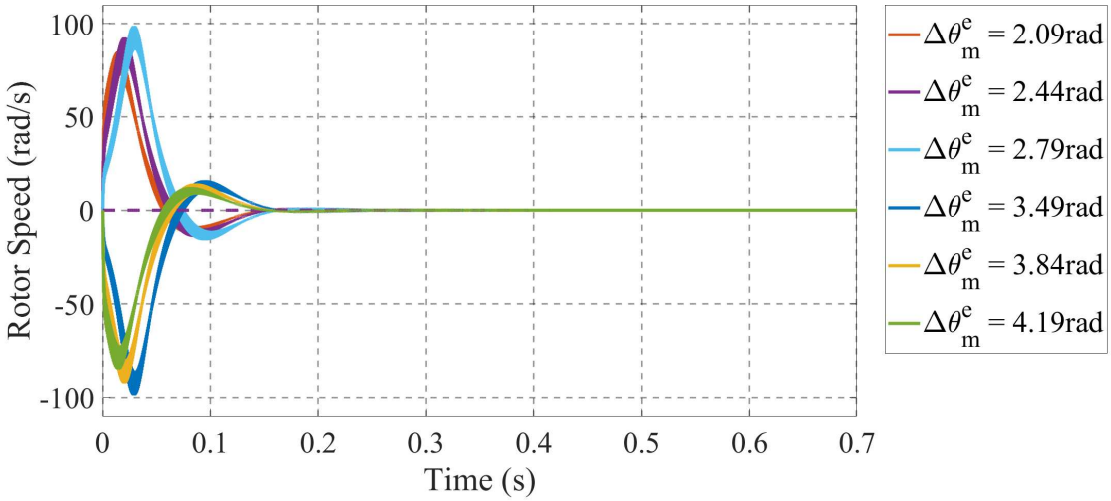


Figure 7.8: Measured (dashed) versus estimated speed for zero-speed rotor injection estimation method with an initial position in proximity of $\theta_{me} = \pi$

This phenomenon is explained by comparing equations (3.16) and (4.6) together, respectively the outcome of the low pass filtering procedure applied on

the demodulation step in the stator injection method and in the rotor injection. In the former method, the q-axis current varies with the sine of twice the estimation error $\hat{\theta}_m^e$, while for the latter observer, the q-axis current varies with the reconstruction error. Hence the rotor injection method shows higher sensibility when performing the zero-speed estimation tasks.

# 8

# Preliminary Experimental Validation

This chapter presents the exploratory experimental setup used for the validation of the theoretical results. The aim of this validation is to report how the nonidealities and the error in the motor parameter estimation process affect the validation procedure in a prototype setup. Therefore this chapter focuses on proving the most important features of the observer discussed in the former chapters. The outcome of these experiments regarding the behavior of the low-speed position observer for both stator and rotor injection methods is reported in the figures of this chapter.

## 8.1 Experimental setup

Figure 8.1 shows the experimental setup, composed of:

- the HEPM motor;
- an auxiliary IPM motor connected to the HEPM motor shaft;
- the stator winding inverter;
- the rotor winding inverter;
- various current measure devices and power supplies;
- an encoder;

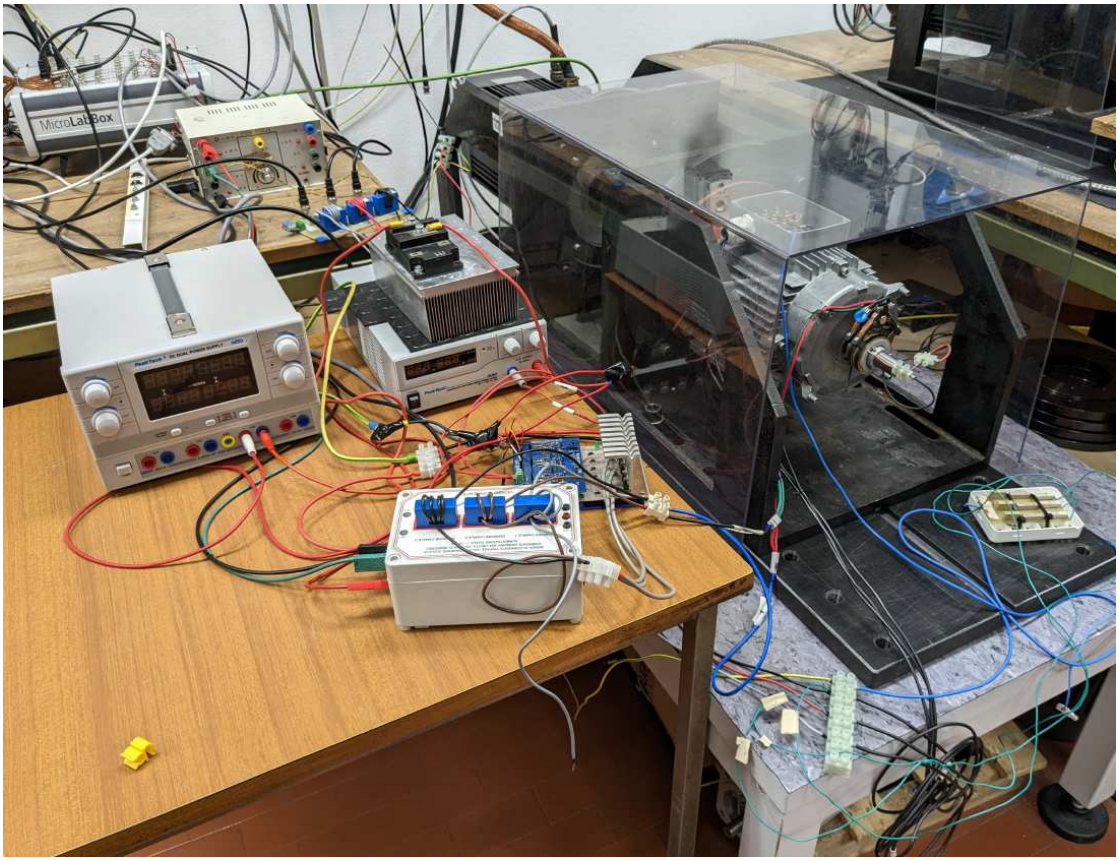


Figure 8.1: Experimental setup

The encoder measures the speed and the position of both motors. The IPM motor is driven by its inverter and is used in this setup to simulate external loads. Moreover thanks to this motor, it is possible to drive the HEPM motor shaft without any control current flowing in it. This feature is used for the low-speed validation procedure. All the inverters and the measurement devices interact with a dSpace MicroLabBox board, allowing the control of the system thanks to the Simulink c-code generator.

## 8.2 Experimental results

Figure 8.2 and 8.3 show the d-q-e currents propagated inside the rotor and the excitation windings due to the high-frequency injection voltage. The former figure reports the effect of the stator injection. The latter figure reports the effect of the rotor injection. These currents are computed by applying the Park transform to the $\alpha - \beta$ currents using the measured position coming from the

encoder. As reported in the figures the current behaviors are not the same as the simulation outcomes, as reported in Figure 5.3 and 5.16. This is probably caused by the difference between the motor parameters estimation, used for the mathematical model, and those of the motor. Furthermore, also the preliminary setup nonidealities and the experimental setup itself might be affecting the current waveforms.

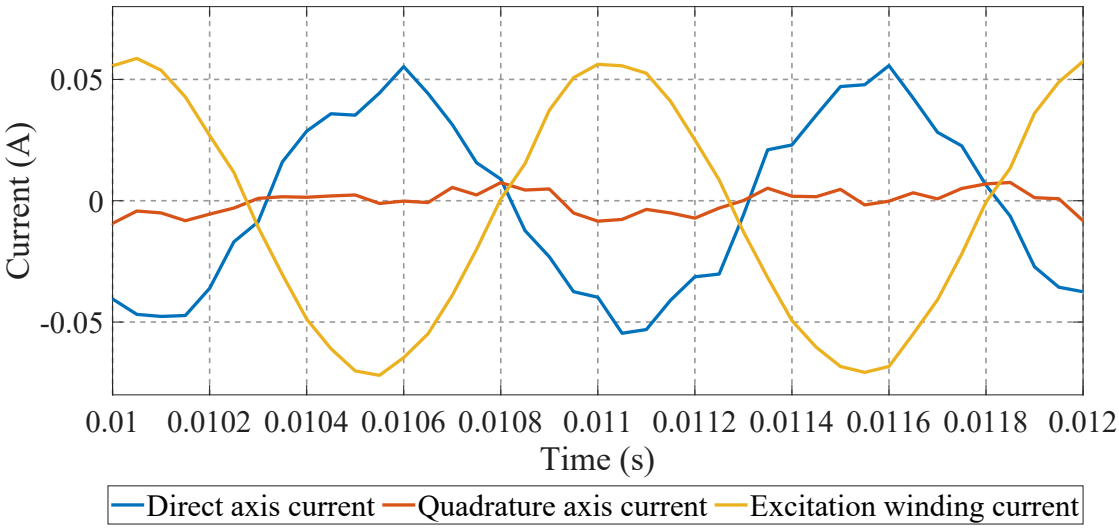


Figure 8.2: Current propagated inside the experimental setup due to the stator voltage injection

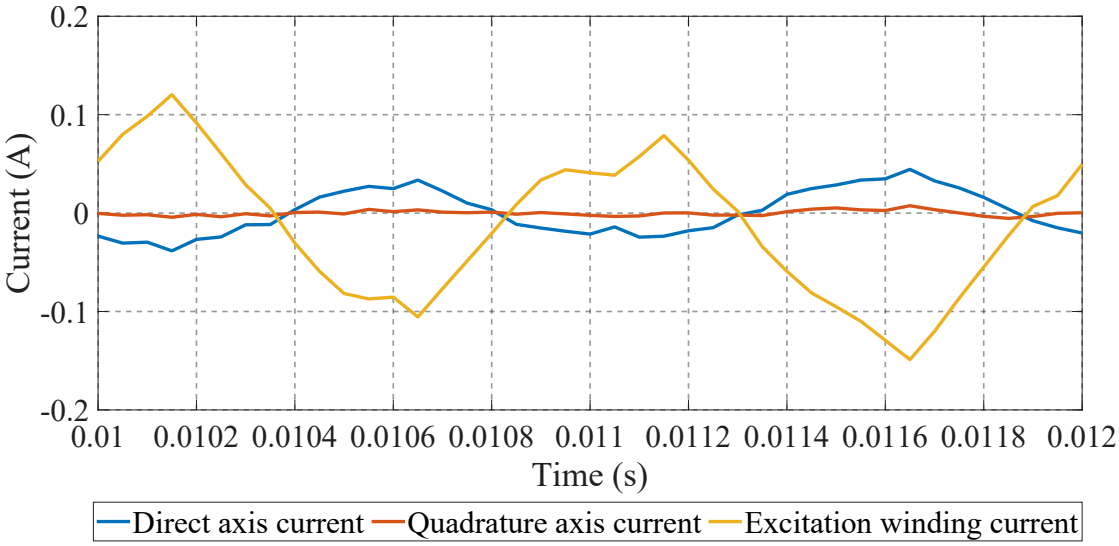


Figure 8.3: Current propagated inside the experimental setup due to the stator voltage injection

However, since also in the experimental setup the q-axis current tends to

be zero when the Park transform is computed with the true position, the key idea behind both estimation methods is still valid. Figure 8.4 and 8.5 shows the position reconstruction compared to the position measured by the encoder respectively observed with the stator and the rotor injection estimation methods.

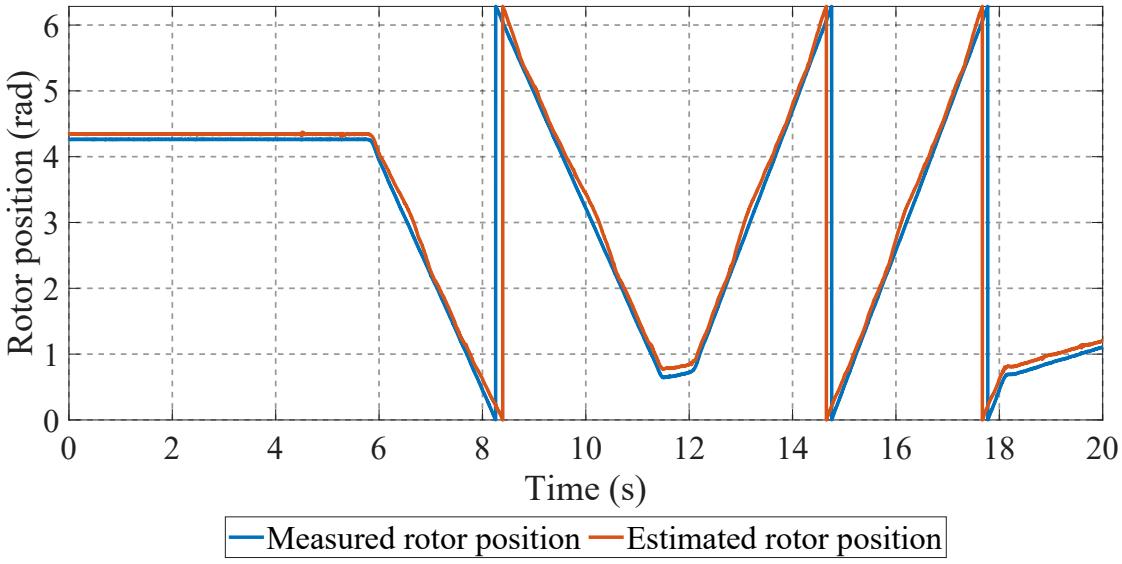


Figure 8.4: Measured position compared to the estimated position coming from the stator injection observer while the HEPM motor is driven by the load motor

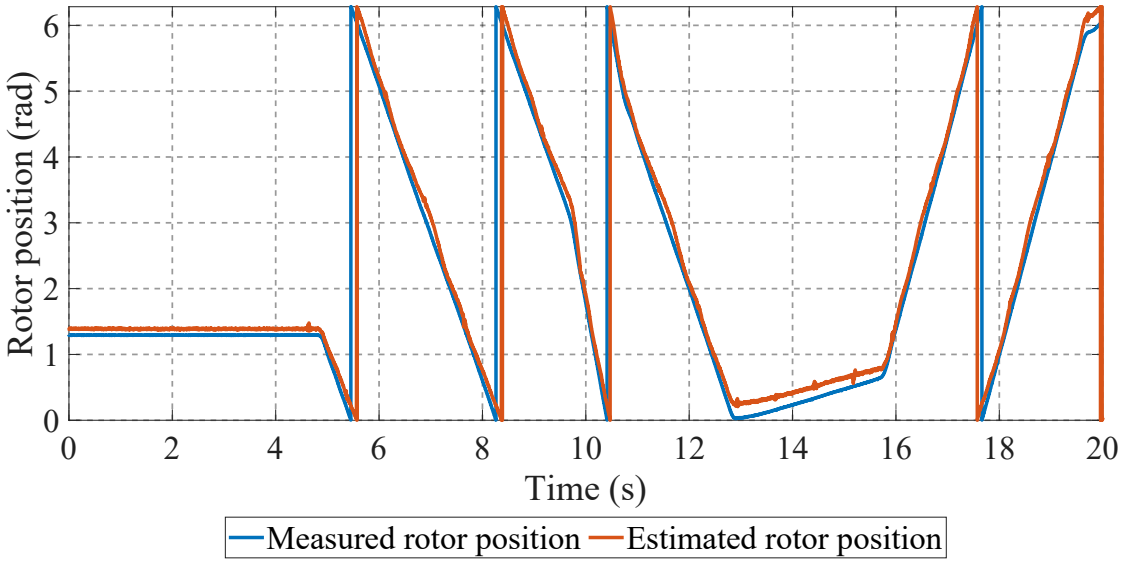


Figure 8.5: Measured position compared to the estimated position coming from the rotor injection observer while the HEPM motor is driven by the load motor

The rotor position reconstruction is achieved. The estimation error maintains a constant behavior while the HEPM control current remains constant. This

error is indeed in correlation with the cross-coupling inductances and depends on the motor operating point. Figure 8.6 and 8.7 report the measured motor shaft velocity compared with the speed observed respectively from the stator injection and the rotor injection estimators. The low-speed reconstruction task is achieved. However, the estimated velocity presents oscillations despite the filtering action performed on the observer outcome.

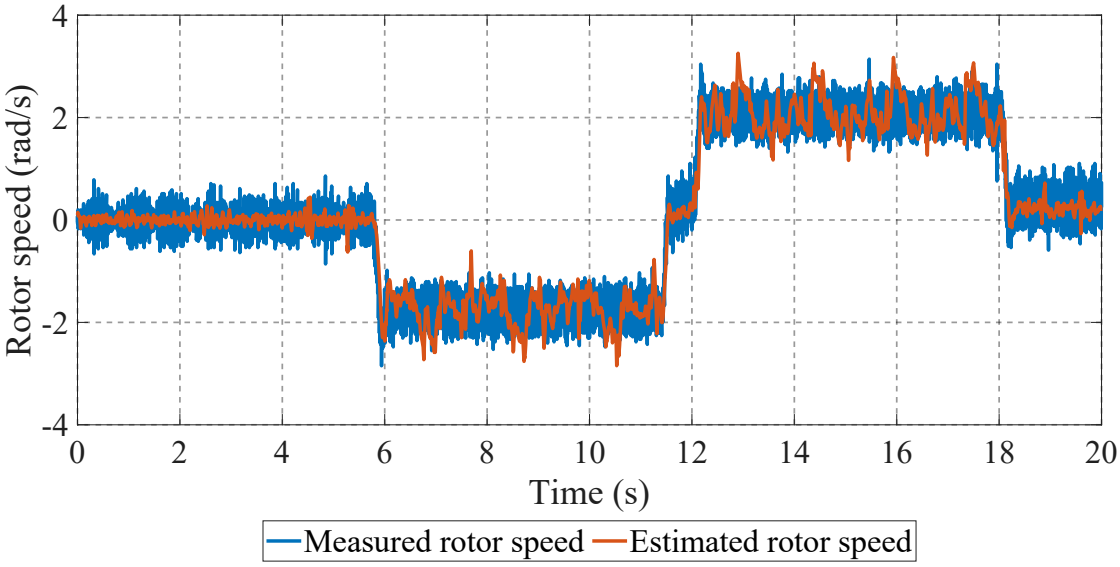


Figure 8.6: Measured speed compared to the estimated speed coming from the stator injection observer while the HEPM motor is driven by the load motor

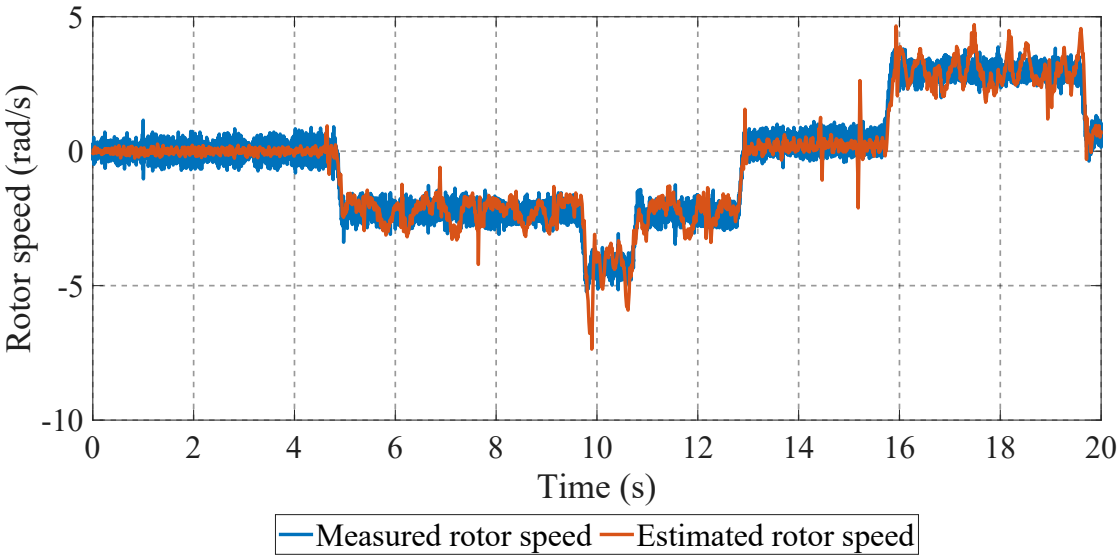


Figure 8.7: Measured speed compared to the estimated speed coming from the rotor injection observer while the HEPM motor is driven by the load motor

Follows up the experimental results of the estimation error predictor. As reported in Figure 8.8 the experimental results are different from the simulation results. Indeed the rotor injection method is characterized by the highest error even though the predicted error of this method is lower than the error prediction coming from the stator injection method. Therefore performing the position estimation error correction in this exploratory experimental setup does not represent a solid strategy.

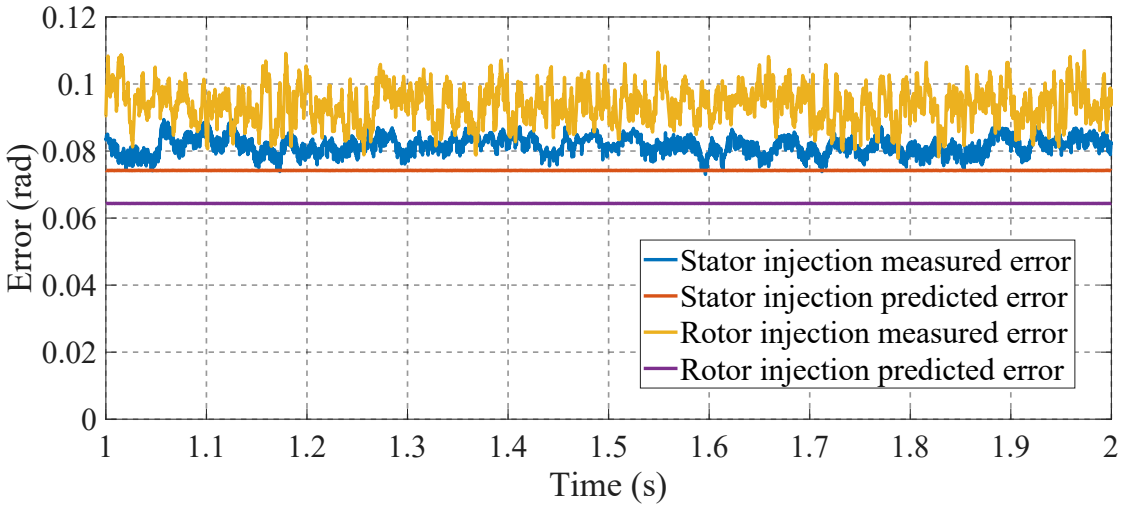


Figure 8.8: Experimental confrontation between the actual position reconstruction error and the predicted one from equations (5.4) and (5.7)

Anyway, since the position error is small compared to the measure, the control action on the rotor velocity using as feedback measures the estimated speed and position is still feasible. The reference frame estimation error is indeed compensated by the control under a certain threshold. However, for this initial experimental setup, this feature is only working for the stator injection method. Figure 8.9 reports the control behavior obtained with a reference speed of 5rad/s. This velocity is near 5% of the base speed and corresponds also to the speed used as speed reference in the simulations. Although the speed reference is reached, the time response of the controlled system is not comparable with the design one. The parameters used for the control design do not take into account the inertia increase due to the auxiliary motor shaft. On the other hand, the perpetual oscillation around the reference point and the shape of the estimated speed suggests that the filtering action performed in the estimated velocity feedback may be improved. Moreover, this non-ideal behavior of the step response may probably be due to the estimation error affecting the position

estimation used as input for the Park transform. On the other hand Figure 8.10 shows the comparison between the estimation error and the prediction coming from (5.4) while the HEPM rotor speed is controlled by feedback with the estimated state. Also in this case the prediction algorithm isn't tracking the estimation error.

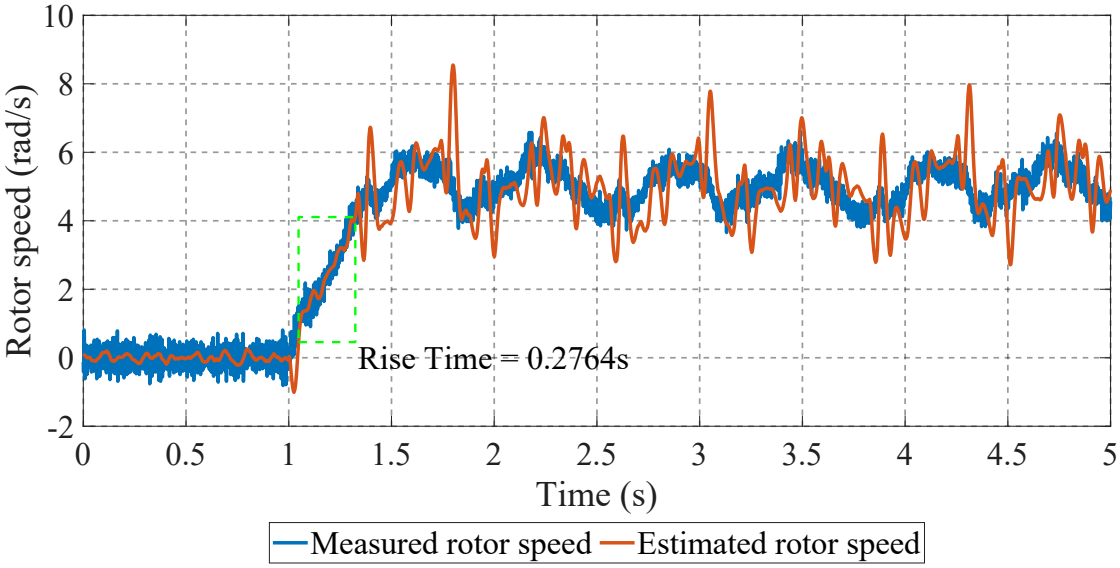


Figure 8.9: Experimental confrontation between the measured position and the stator injection reconstruction when the observed state is used as feedback for the speed control


Figure 8.10: Experimental confrontation between the measured position error and the error coming from the stator injection method prediction formula when the observed state is used as feedback for the speed control

# 9

# Conclusions

This thesis provides the mathematical results that led to the design of a low-speed sensorless technique for the reconstruction of the rotor mechanical state of an Hybrid Excitation Permanent Magnet (HEPM) motor. In particular, this work provides also an in-depth comparison between two high-frequency voltage injection techniques: the stator injection method, and the rotor injection method. The former has been considered state-of-the-art because of its performance when used in sensorless techniques for anisotropic motor applications. This method has been proven to be a valid technique also for HEPM motor applications. The latter estimation technique has been proposed in this work since it is a feasible observer strategy for HEPM motors thanks to the rotor winding. Moreover, the proposed method injects a current axis that is invariant to the Park transform since is synchronous to the magnetic field direction of the rotor permanent magnets for construction. Hence unlike the stator method that injects the high-frequency voltage in an estimated axis, the rotor method always injects the high-frequency voltage without being affected by the estimation error. Therefore the latter method is supposed to have less error in the estimation procedure. In conclusion, for low-speed operating scenarios, sensorless estimation techniques offer a feasible alternative to conventional sensor-based methods also for HEPM motors. The simulations on the mathematical model provide an initial validation of this fact. Both estimation methods are indeed reconstructing the rotor mechanical state. Hence adopting the speed control architecture discussed in Chapter 6 the control of the shaft mechanical speed with feedback on the estimated mechanical state is achieved. However, to design a position

control architecture in-depth work has to be done: as widely discussed in this work this kind of application presents an estimation error that depends on the motor operation point. Eventually, both estimators represent valuable solutions to the sensorless zero-speed and low-speed estimation. However, the rotor injection method offers slight advantages in performance. The results obtained from the preliminary experiments reported in the last chapter of this work proved the consistency of this method. Hence, although the discrepancies between the motor model used in the simulation and the real motor plus the nonidealities introduced in the experimental setup, the zero-speed and low-speed estimation of the rotor position and velocity have been achieved. However the experimental results show that to reach the simulation performances also in the experimental setup, in-depth knowledge of motor parameters and accurate tests on both filtering and current measures strategies are mandatory. Especially if the final aim for the observer is to provide a reconstruction for high-precision position control applications. Future works for this research may consist of the construction of an improved experimental setup that can consistently validate the results obtained with the simulation setup and the explorative test on the HEPM motor provided by this research.

# 10 Appendix

## 10.1 Differential inductance matrix inversion

Starting with the matrix defined as in equation (3.2), we compute the determinant (10.1):

$$\begin{aligned}\Delta_l &= l_{dd}l_{qq}l_e - \frac{3}{2}l_q l_{de}^2 - l_{ee}l_{dq}^2 + 3l_{de}l_{qe}l_{dq} - \frac{3}{2}l_{dd}l_{qe}^2 \\ &= \frac{l_{qq}}{2}\left[(-3l_{de}^2 + 2l_{dd}l_e) + \left(-2\frac{l_{ee}l_{dq}^2}{l_{qq}}\right) + \left(6\frac{l_{de}l_{dq}lqe}{l_{qq}} - 3\frac{l_{dd}l_{qe}^2}{l_{qq}}\right)\right] \\ &= \frac{l_{qq}}{2}(\alpha+\beta+\gamma) = \frac{l_{qq}}{2}\sigma\end{aligned} \tag{10.1}$$

For this particular motor, the determinant is not zero. Hence, also in the simplified case where both the q-e mutual induction and the magnetic cross saturation are neglected, $\beta$ and $\gamma$ are equal to zero, meaning that $\gamma = \alpha$. HEPM Motor parameter grants that the determinant of the l matrix is different from zero. This means that the l matrix is invertible and matrix $l^{-1}$ exists. The adjugate matrix is computed in (10.2).

$$Adj_l = \begin{bmatrix} l_{qq}l_e - \frac{3}{2}l_{qe}^2 & \frac{3}{2}l_{de}l_{qe} - l_{dq}l_{ee} & l_{dq}l_{qe} - l_{de}l_q \\ \frac{3}{2}l_{de}l_{qe} - l_{dq}l_{ee} & l_{dd}l_{ee} - \frac{3}{2}l_{de}^2 & l_{de}l_{dq} - l_{dd}l_{qe} \\ \frac{3}{2}l_{dq}l_{qe} - \frac{3}{2}l_{de}l_{qq} & \frac{3}{2}l_{de}l_{dq} - \frac{3}{2}l_{dd}l_{qe} & l_{dd}l_{qq} - l_{dq}^2 \end{bmatrix} \tag{10.2}$$

Then the inverse is then computed thanks to (10.3)

$$l^{-1} = \frac{Adj_l}{\Delta_l} = \frac{2}{l_{qq}\sigma} Adj_l = \\ = \frac{1}{l_{qq}\sigma} \begin{bmatrix} 2l_e l_{qq} - 3l_{qe}^2 & 3l_{de}l_{qe} - 2l_{dq}l_e & 2l_{dq}l_{qe} - 2l_{de}l_q \\ 3l_{de}l_{qe} - 2l_{dq}l_e & 2l_{dd}l_e - 3l_{de}^2 & 2l_{de}l_{dq} - 2l_{dd}l_{qe} \\ 3l_{dq}l_{qe} - 3l_{de}l_{qq} & 3l_{de}l_{dq} - 3l_{dd}l_{qe} & 2l_{dd}l_{qq} - 2l_{dq}^2 \end{bmatrix} \tag{10.3}$$

## 10.2 MATLAB CODE FOR CURRENT DERIVATION

```
clc;
clear variables;
close all;

% Differential inductances
ld = sym("ld");
lq = sym("lq");
le = sym("le");
ldq = sym("ldq");
lde = sym("lde");
lqe = sym("lqe");

% Injection params
delta_th = sym("Dth");
w = sym("whf");
U_hf = sym("Uhf");

l_matrix = [ld, ldq, lde;...
            ldq, lq, lqe;...
            (3/2)*lde, (3/2)*lqe, le];

% Inverse matrix computation
disp("Inductance matrix");
disp(l_matrix);

```

```
26 disp("Inductance matrix adjoint");
27 adj = adjoint(l_matrix);
28 disp(adj);
29
30 delta = det(l_matrix);
31 disp("Inductance matrix determinant");
32 disp(delta);
33
34 sym_sigma = sym("s");
35 disp("Inductance matrix inverse with sigma term");
36 l_inv = 2*adj/(lq*sym_sigma);
37 disp(l_inv);
38
39 %% Delta theta to Iqhf relation:
40
41 % Rotation Matrices
42 dqe_hat2dqe = [cos(delta_th), +sin(delta_th), 0;...
43                -sin(delta_th), cos(delta_th),  0;...
44                   0,            0,        1];
45
46 dqe2dqe_hat = [ cos(delta_th),  -sin(delta_th), 0;...
47                 sin(delta_th), cos(delta_th),   0;...
48                        0,            0,        1];
49
50 % Rotor Injection
51 disp("ROTOR INJECTION METHOD");
52 disp("");
53 curr = sin(w);
54 inj_vector_ri = [0;...
55                  0;...
56                  U_hf*curr/w];
57
58 ihdqe_ri = l_inv*inj_vector_ri;
59 disp("Injected current");
60 disp(ihdqe_ri);
61
```

```
rot_ihdqe_ri = dqe2dqe_hat*ihdqe_ri;
disp("Delta theta rotated ihdqe");
disp(rot_ihdqe_ri);

rot_ihfq_ri = rot_ihdqe_ri(2);
demod_ihfq_ri = rot_ihfq_ri*curr;
disp("Estimated Iqhf");
disp(simplify(collect(demod_ihfq_ri)));

%% Stator Injection
inj_vector_si = [U_hf*curr/w;...
                 0;...
                 0];

disp("STATOR INJECTION METHOD");
disp("");

s_vdq_inj_int = dqe_hat2dqe*inj_vector_si;
disp("true dq injected voltage");
disp(s_vdq_inj_int);

s_i_dq_hf = l_inv*s_vdq_inj_int;
disp("Stator injection true idq hf")
disp(simplify(collect(s_i_dq_hf)));

s_i_dq_hat_hf = dqe2dqe_hat * s_i_dq_hf;
disp("Stator injection estimated iq hf")
s_simp_iqhf = simplify(collect(s_i_dq_hat_hf(2)));
disp(s_simp_iqhf);
```

# Bibliography


[1] D Plusa et al. "On the magnetic properties of bonded magnets made from a mixture of Nd (Fe, Co) B and strontium ferrite or alnico powder". In: *Rev. Adv. Mater. Sci* 18 (2008), pp. 541–544.

[2] JF Herbst and JJ Croat. "Neodymium-iron-boron permanent magnets". In: *Journal of magnetism and magnetic materials* 100.1-3 (1991), pp. 57–78.

[3] Jian-Hong Yi. "Development of samarium–cobalt rare earth permanent magnetic materials". In: *Rare Metals* 33.6 (2014), pp. 633–640.

[4] Jacek F Gieras. *Permanent magnet motor technology: design and applications*. CRC press, 2009.

[5] Sen Li. "A review of electric motor drives for applications in electric and hybrid vehicles". In: *Researchgate, March* (2017).

[6] Daniele Michieletto, Luca Cinti, and Nicola Bianchi. "Hybrid Excitation PM Synchronous Motors: Part I – Per Unit Analysis". In: *IEEE Transactions on Energy Conversion* 37.1 (2022), pp. 487–494. DOI: 10.1109/TEC.2021.3107937.

[7] Daniele Michieletto, Luca Cinti, and Nicola Bianchi. "Hybrid Excitation PM Synchronous Motors: Part II — Finite Element Analysis". In: *IEEE Transactions on Energy Conversion* 37.1 (2022), pp. 495–504. DOI: 10.1109/TEC.2021.3107957.

[8] Luca Cinti et al. "A Comparison between Hybrid Excitation and Interior Permanent Magnet Motors". In: (2021), pp. 10–15. DOI: 10.1109/WEMDCD51469.2021.9425634.

[9] Ludovico Ortombina et al. "Comprehensive Analysis and Design of a Pulsating Signal Injection-Based Position Observer for Sensorless Synchronous Motor Drives". In: *IEEE Journal of Emerging and Selected Topics in*

*Power Electronics* 10.2 (2022), pp. 1925–1934. DOI: 10.1109/JESTPE.2021.3053467.

[10] David Reigosa et al. "Sensorless control of wound rotor synchronous motors based on rotor high-frequency signal injection". In: *IEEE Transactions on Industry Applications* 57.6 (2021), pp. 6034–6043.

[11] Paolo Gherardo Carlet et al. "Dynamic model for HEPM motors including the nonlinear magnetic characteristics". In: (2023), pp. 1–7. DOI: 10.1109/IEMDC55163.2023.10239046.

[12] Matteo Berto et al. "Computation of Self-Sensing Capabilities of Synchronous Machines for Rotating High Frequency Voltage Injection Sensorless Control". In: *IEEE Transactions on Industrial Electronics* 69.4 (2022), pp. 3324–3333. DOI: 10.1109/TIE.2021.3071710.

[13] Matteo Berto et al. "An Effective Ellipse Fitting Technique of the Current Response Locus to Rotating HF Voltage Injection in IPMSM for Sensorless Rotor Position Estimation". In: *IECON 2018 - 44th Annual Conference of the IEEE Industrial Electronics Society*. 2018, pp. 391–396. DOI: 10.1109/IECON.2018.8591855.

[14] M.J. Corley and R.D. Lorenz. "Rotor position and velocity estimation for a salient-pole permanent magnet synchronous machine at standstill and high speeds". In: *IEEE Transactions on Industry Applications* 34.4 (1998), pp. 784–789. DOI: 10.1109/28.703973.

[15] Luca Cinti et al. "Maximization of Sensorless Capabilities of Hybrid Excited Permanent Magnet Motors". In: (2022), pp. 2234–2241. DOI: 10.1109/ICEM51905.2022.9910877.

[16] Virginia Manzolini, Mattia Morandin, and Silverio Bolognani. "The crowded axis of the frequency: Optimal pole/zero allocation for a full speed sensorless synchronous motor drives". In: (2016), pp. 1–8.